UNIVERSITY OF AMSTERDAM

MSc Physics

Track: Theoretical Physics

MASTER THESIS

Finite bond dimension scaling with the corner transfer matrix renormalization group method

Geert Kapteijns

10275037

July 2017

60 ECTS

Supervisor:
Dr. Philippe Corboz

Examiner:
Prof. dr. Bernard Nienhuis

Institute for Theoretical Physics

Abstract

This thesis investigates scaling in the number of basis states kept (the *bond dimension* m) in approximating the partition function of two-dimensional classical models with the corner transfer matrix renormalization group (CTMRG) method.

For the Ising model, it is shown that exponents and the transition temperature may be approximated with a scaling analysis in the correlation length defined in terms of the row-to-row transfer matrix at the (pseudo)critical point, as was suggested by Nishino et al. However, the calculated quantities show inherent deviations from the basic scaling laws, due to the spectrum of the underlying corner transfer matrix (CTM). These deviations are mitigated to some extent when we define the correlation length in terms of the classical analogue of the entanglement entropy. Scaling directly in the bond dimension m is also possible, but less accurate since the law for the correlation length $\xi \propto m^{\kappa}$ holds only in the limit $m \to \infty$ and does not take into account the spectrum of the CTM that is obtained.

It is found that finite-m scaling and finite-size scaling yield comparable accuracy for critical exponents and the transition temperature. With finite-m scaling larger effective system sizes are obtainable, but finite-size approximations do not suffer from the deviations due to the CTM spectrum and are consequently of higher quality. Therefore it is plausible that finite-size results will improve significantly if corrections to scaling are included in the fits.

We also present a numerical analysis of the clock model with $q = \{5, 6\}$ states, concluding that the Kosterlitz-Thouless picture is plausible. We find values of the transition temperatures that are in agreement with values found by other authors. Results for the exponent η indicate that the critical temperatures found in both this study and previous work might be too close together. It is conceivable that, after considering larger systems and taking into account finite-size corrections, both critical temperatures and the values of η will be adjusted outwards towards their true values, thereby completely reconciling the results.

Overall, we conclude that finite-m scaling is a valuable alternative to finite-size scaling within CTMRG, since larger system sizes are accessible. The CTMRG analysis is itself a valuable addition to other approximation methods such as Monte Carlo, yielding comparable results, while obtaining estimates from completely different principles. Furthermore it reveals information, such as the the spectrum of the transfer matrices and the central charge of the massless phase, that is not accessible otherwise.

Contents

Acknowledgements vi

1 Introduction 1
- 1.1 Statistical mechanics and phase transitions . . . 2
  - 1.1.1 Universality . . . 2
- 1.2 Baxter's method as a precursor to tensor network methods . . 3
- 1.3 Structure of this thesis . . . 4

2 Density matrix renormalization group method 5
- 2.1 Introduction . . . 5
- 2.2 Density matrix renormalization group . . . 6
  - 2.2.1 Real-space renormalization group . . . 6
  - 2.2.2 Single particle in a box . . . 7
  - 2.2.3 Density matrix method . . . 7
  - 2.2.4 Infinite-system method . . . 9

3 DRMG applied to two-dimensional classical lattice models 12
- 3.1 Statistical mechanics on classical lattices . . . 12
- 3.2 Transfer matrices of lattice models . . . 13
  - 3.2.1 1D Ising model . . . 13
    - 3.2.1.1 Fixed boundary conditions . . . 15
  - 3.2.2 2D Ising model . . . 16
- 3.3 Partition function of the 2D Ising model as a tensor network . 17
  - 3.3.1 Tensor network of the partition function of a system of four spins . . . 18
  - 3.3.2 Thermodynamic limit . . . 18
  - 3.3.3 The transfer matrix as a tensor network . . . 20
- 3.4 Transfer matrix renormalization group . . . 20
  - 3.4.1 The infinite system algorithm for the transfer matrix . 22
  - 3.4.2 Physical interpretation of the reduced density matrix . 23
- 3.5 Corner transfer matrix renormalization group . . . 25
  - 3.5.1 Corner transfer matrices . . . 25
  - 3.5.2 Corner transfer matrix as a tensor network . . . 25

3.5.3 Corner transfer matrix renormalization group method 26
3.5.3.1 Equivalence to TMRG and DMRG in the thermodynamic limit . . . 27
3.6 Calculation of observable quantities . . . 29
3.6.1 Free energy per site . . . 29
3.6.2 Magnetization per site . . . 29
3.6.3 Analogy to entanglement entropy for classical systems 30
3.7 Spectrum of the corner transfer matrix . . . 31
3.7.1 Analytical results for the Ising model . . . 31
3.7.2 Implications for finite-m simulations . . . 32
3.8 Equivalence to variational approximation in the space of matrix product states. . . . 33

4 Critical behaviour and finite-size scaling 34
4.1 Phase transitions . . . 34
4.1.1 Finite systems . . . 35
4.2 Critical behaviour . . . 35
4.2.1 Finite-size scaling . . . 36
4.2.1.1 The finite-size scaling ansatz . . . 38
4.2.1.2 Extracting exponents from numerical simulation . . . 39

5 Finite-m scaling in the CTMRG algorithm 41
5.1 Introduction . . . 41
5.2 Definition of the effective length scale in terms of the correlation length at T_c . . . 42
5.3 Relation to finite-entropy scaling and the exponent κ. . . . 43
5.3.1 Quantitative theory for κ . . . 44
5.4 Locating the critical point with the entanglement spectrum . . 46

6 Technical details and convergence behaviour 48
6.1 Symmetricity and normalization of tensors . . . 48
6.2 Boundary conditions . . . 49
6.3 Convergence criteria . . . 49
6.3.1 Simulations with finite bond dimension . . . 49
6.3.1.1 Convergence at the critical point of the Ising model . . . 49
6.3.2 Simulations with finite system size . . . 50
6.4 Values of hyperparameters for the Ising model . . . 54

7 Numerical results for the Ising model 57
7.1 At the critical point . . . 57
7.1.1 Existence of two length scales . . . 57
7.1.2 Central charge . . . 60
7.1.3 Using the entropy to define the correlation length . . . 61
7.1.4 Exponent κ . . . 61
7.1.4.1 Comparison with exact result in asymptotic limit . . . 63
7.2 Locating the critical point . . . 63
7.2.1 Finite m . . . 64
7.2.2 Finite N . . . 66
7.3 Away from the critical point . . . 66
7.4 Discussion . . . 70
7.4.1 Finite-m vs finite-size simulations . . . 70
7.4.2 Exponent κ . . . 71

8 Numerical results for the clock model 72
8.1 Introduction . . . 72
8.2 Previous numerical results . . . 74
8.2.1 The $q = 5$ clock model . . . 74
8.2.2 The $q = 6$ clock model . . . 75
8.3 Spectrum of the corner transfer matrix . . . 76
8.4 Magnetization . . . 76
8.5 Classical analogue to the entanglement entropy . . . 77
8.6 Transition temperatures . . . 78
8.6.1 Numerical difficulties with finite-m simulations around T_1 . . . 81
8.6.2 Transition from the ordered to the massless phase T_1 . . . 81
8.6.3 Transition from the massless to the disordered phase T_2 82
8.6.3.1 Finite-size scaling . . . 82
8.6.3.2 Finite-m scaling . . . 83
8.7 The massless phase . . . 84
8.7.1 Central charge . . . 84
8.7.2 Varying exponent for the magnetization . . . 85
8.8 Discussion . . . 88
8.8.1 Finite-size effects . . . 88
8.8.2 Other means of studying the transitions T_1 and T_2 . . . 91

9 Conclusions 93

A Correspondence of quantum and classical lattice systems **96**

B Introduction to tensor networks **98**
B.1 Tensors, or multidimensional arrays 98
B.2 Tensor contraction 99
B.3 Tensor networks 99
B.3.1 Graphical notation 100
B.3.2 Reshaping tensors 101
B.3.3 Computational complexity of contraction 101

Bibliography **103**

Acknowledgements

I want to thank Philippe Corboz for all his help during the past year. Thanks for being always enthusiastic and ready to answer questions, for including me in the group from the start, and for showing me the messy reality of research.

Thanks to Piotr Czarnik, Sangwoo Chung, Schelto Crone, Karel Temmink and Ido Niesen for many helpful discussions. Especially Ido, who took more time to help me than could have reasonably been expected of someone with such a busy schedule.

Thanks to Bernard Nienhuis, for very helpful discussions towards the end of my thesis.

Thanks to Tobias Bouma, for good times and for sharing your arcane knowledge of LaTeX.

Thanks to Boris Ponsioen for the hours and hours we spent drinking coffee, discussing the intricacies of this-or-that algorithm or our next career move. Those significantly broadened my perspective.

Thanks to Daan Mulder for our discussions about physics, politics and music. If I remembered one line of a song, you could always declaim the whole verse, at least in the case of Cohen (may he rest in peace).

Thanks to my family, whom I didn't see much the past year. And finally, thanks to Marianne.

1
Introduction

This thesis investigates a numerical approximation method put forth by Baxter in 1978 [1–3] based on the corner transfer matrix formulation of the partition function for two-dimensional classical lattice models.

The method rose to prominence in 1996, under the name *corner transfer matrix renormalization group* (CTMRG), when Nishino and Okunishi showed [4] that in the thermodynamic limit, it is equivalent to the hugely successful density matrix renormalization group (DMRG) method for one-dimensional quantum systems [5] (discovered in 1992 by White), which does not suffer from the *negative sign problem* [6] that makes Monte Carlo sampling of frustrated or fermionic systems infeasible.

The error in the CTMRG method comes from the fact that the corner transfer matrices, whose dimension diverges exponentially in the lattice size, have to be truncated at a maximum dimension m in order to make numerical manipulation possible. This finite *bond dimension* m (also denoted by χ or D in the literature) introduces finite-size effects, comparable to those observed for systems that are finite in one or more spatial dimensions. This was already realized by Nishino et al. [7].

The goal of this thesis is twofold: (i) investigate how *finite bond dimension scaling* may be performed with the CTMRG algorithm for classical systems, where we can directly compare it with finite-size scaling, and (ii) investigate how it compares to other numerical approaches, such as Monte Carlo, in a difficult scenario.

For (i), I have studied the Ising model, for which all results may be checked against the exact solution. For (ii), I have studied the clock model with $q = \{5, 6\}$ states, which is regarded as difficult numerically and subject to some controversy.

Before the structure of this thesis is laid out, I will first make some general remarks on statistical mechanics and phase transitions, and on how the

CTMRG method relates to the class of newer methods for simulating many-body systems that grew out of White's breakthrough, known as *tensor network algorithms*.

1.1 Statistical mechanics and phase transitions

Statistical mechanics is concerned with describing the average properties of systems consisting of many particles. Examples of such systems are the atoms making up a bar magnet, the water molecules in a glass of water, or virtually any other instance of matter around us.

Matter can arrange itself in various structures with fundamentally different properties. We call these distinct states of matter *phases*. When matter changes from one phase to another, we say it undergoes a phase transition.

Physics has made great strides in understanding these transitions. The complete history of the field is beyond the scope of this introduction and this thesis, but the reader may wish to consult [8, 9] to get an idea.

Only as late as 1936, the occurrence of a phase transition within the framework of statistical physics was established by R. Peierls [10]. He showed that the two-dimensional Ising model has a non-zero magnetization for sufficiently low temperatures. Since for high enough temperatures the Ising model loses its magnetization, it follows that there must be phase transition in between.

The effort to understand the Ising model culminated with Onsager's exact solution in 1944 [11], which rigorously established a sharp transition point in the thermodynamic limit. In the years that followed, more models were exactly solved. Examples are the spherical model [12] (1952), ice-type models [13] (1967) and the eight-vertex model [14] (1971). A pedagogical treatment of these and other models can be found in [15].

In the meantime, various approximation methods were developed. With rapidly improving computers, the method of statistical sampling (Monte Carlo) became one of the most prominent and its significance has not waned. Other methods are, among others, series expansions and variational approximations. A variational approximation put forth by Kramers and Wannier (1941) [16] was later seen to be equivalent to Baxter's corner transfer matrix method with $m = 2$.

1.1.1 Universality

One may question the relevance of studying very simple models such as the Ising model. As it turns out, systems that are at first sight vastly different may

show qualitatively similar behaviour near a phase transition. For example, exponents that characterize the divergence of quantities near a transition are conjectured to be independent on microscopic details of the interactions between particles, but instead fall into distinct *universality classes* [17, 18]. Thus, studying the very simplest model may yield universal results.

1.2 Baxter's method as a precursor to tensor network methods

Baxter showed that the optimal truncation of corner transfer matrices corresponds, in the thermodynamic limit, to a variational optimization of the row-to-row transfer matrix within a certain subspace, now known as the subspace of *matrix product states* (MPSs) [2, 19].

After the success of White's DMRG, which, as Nishino and Okunishi pointed out, is equivalent to Baxter's method, the underlying matrix-product structure was rediscovered in the context of one-dimensional quantum systems by Östlund and Rommer [20, 21].

It is historically significant but little known that Nightingale, in a footnote of a 1986 paper [22], already made the remark that "The generalization [of Baxter's method] to quantum mechanical systems is straightforward."

After Östlund and Rommer, it was realized that reformulating White's algorithm directly in terms of matrix product states provided the explanation of the algorithm's shortcomings around phase transitions. An MPS-ansatz fundamentally limits the entropy of the ground state approximation and since the entropy diverges at a conformally invariant critical point [23], DMRG gives inaccurate results.

This gave rise to other ansätze, formulated in the language of tensor networks [24], specifically designed to represent states with a certain amount of entropy. Examples are multi-scale entanglement renormalization ansatz (MERA) for critical one-dimensional quantum systems [25] and projected entangled-pair states (PEPS) [26] for two-dimensional quantum systems.

Other tensor network algorithms, such as infinite time-evolving block decimation [27] in one dimension and iPEPS (infinite PEPS) [28] in two dimensions made it possible to directly approximate quantum systems in the thermodynamic limit.

iTEBD was used to study finite bond dimension scaling (under the slightly different name of *finite-entropy scaling*) [29]. Some theoretical predictions were later made in [30].

1.3 Structure of this thesis

It is in the mostly quantum-oriented research field sketched above that the work for this thesis was done. Therefore, I have chosen to begin by introducing White's algorithm in its original description (chapter two), before making the connection to two-dimensional classical lattices and properly introducing the corner transfer matrix formulation (chapter three).

In chapter four, the concepts of critical behaviour and finite-size scaling are introduced and in chapter five these concepts are connected to the work already done on finite bond dimension (or finite-entropy) scaling.

Technical details and convergence behaviour of the CTMRG algorithm are reported in chapter six. It is found that the values of observables may be accurately extrapolated in the chosen convergence criterion of the algoritm.

Results for the Ising model are presented and analyzed in chapter seven. With finite-m simulations, it is much easier to reach large system sizes, but thermodynamic quantities do not grow smoothly as a function of the bond dimension, as a result of the underlying spectrum of the corner transfer matrix.

Quantities calculated with finite-size simulations do not suffer this unsmooth behaviour. Results for both methods are comparable, but it is plausible that finite-size data turns out to be more accurate when corrections to scaling are included.

A numerical analysis of the clock model with $q = \{5, 6\}$ states is given in chapter eight. The model has a low-temperature ordered phase, a massless phase and a high-temperature disordered phase. The transition temperatures T_1 and T_2 are located by extrapolating the positions of pseudocritical temperatures, assuming the transitions are of the Kosterlitz-Thouless type. I find slightly contradictory results, based on exact results in a related formulation of the model, but argue it is plausible that this is due to finite-size effects.

2

Density matrix renormalization group method

The density matrix renormalization group, proposed in 1992 by White [5], is introduced in its historical context. To highlight the ideas that led to this method, we explain the real-space renormalization group, proposed by Wilson [31] in 1975. We then explain how the shortcomings of Wilson's method led to the density matrix renormalization group.

2.1 Introduction

Consider the problem of numerically finding the ground state $|\Psi_0\rangle$ of an N-site one-dimensional spin-$\frac{1}{2}$ system. The underlying Hilbert space of the system is a tensor product of the local Hilbert spaces $\mathscr{H}_{\text{site}}$, which are spanned by the states $\{|\uparrow\rangle, |\downarrow\rangle\}$. Thus, a general state of the system is a unit vector in a 2^N-dimensional space

$$|\Psi\rangle = \sum_{\sigma_1,\sigma_2,\ldots\in\{|\uparrow\rangle,|\downarrow\rangle\}} c_{\sigma_1,\sigma_2,\ldots,\sigma_N} |\sigma_1\rangle \otimes |\sigma_2\rangle \otimes \ldots \otimes |\sigma_N\rangle \,. \tag{2.1}$$

For a system with 1000 particles, the dimensionality of the Hilbert space comes in at about 10^{301}, some 220 orders of magnitude larger than the number of atoms in the observable universe. How can we possibly hope to approximate states in this space?

As it turns out, nature is very well described by Hamiltonians that are local – that do not contain interactions between an arbitrary number of bodies. And for these Hamiltonians, only an exponentially small subset of states can be explored in the lifetime of the universe [32]. That is, only exponentially few states are physical. The low-energy states, especially, have special properties that allow them to be very well approximated by a polynomial number

of parameters. This explains the existence of algorithms, of which the density matrix normalization group is the most widely celebrated one, that can approximate certain quantum systems to machine precision.

2.2 Density matrix renormalization group

The density matrix renormalization group (DMRG), introduced in 1992 by White [5], aims to find the best approximation of a many-body quantum state, given that only a fixed amount of basis vectors is kept. This amounts to finding the best truncation

$$\mathscr{H}_N \rightarrow \mathscr{H}_{\text{eff}} \tag{2.2}$$

from the full N-particle Hilbert space to an effective lower dimensional one. This corresponds to renormalizing the Hamiltonian H.

Before DMRG, several methods for achieving this truncation were proposed, most notably Wilson's real-space renormalization group [31]. We will discuss this method first, and highlight its shortcomings, which eventually led to the invention of the density-matrix renormalization group method by White.

2.2.1 Real-space renormalization group

Consider again the problem of finding the ground state of a many-body Hamiltonian H. A natural way of renormalizing H in real-space is by partitioning the lattice in blocks, and writing H as

$$H = H_A \otimes \ldots \otimes H_A \tag{2.3}$$

where H_A is the Hamiltonian of a block.

The real-space renormalization procedure now entails finding an effective Hamiltonian H'_A of the two-block Hamiltonian $H_{AA} = H_A \otimes H_A$. In the method introduced by Wilson, H'_A is formed by keeping the m lowest lying eigenstates $|\epsilon_i\rangle$ of H_{AA}:

$$H'_A = \sum_{i=1}^{m} \epsilon_i \, |\epsilon_i\rangle \langle\epsilon_i| \, . \tag{2.4}$$

This is equivalent to writing

$$H'_A = O H_{AA} O^\dagger, \tag{2.5}$$

with O an $m \times 2^L$ matrix, with rows being the m lowest-lying eigenvectors of H_{AA}, and L the number of lattice sites of a block. At the fixed point of this iteration procedure, H_A represents the Hamiltonian of an infinite chain.

In choosing this truncation, it is assumed that the low-lying eigenstates of the system in the thermodynamic limit are composed of low-lying eigenstates of smaller blocks. It turns out that this method gives poor results for many lattice systems. Following an example put forth by White and Noack [33], we establish an intuition why.

2.2.2 Single particle in a box

Consider the Hamiltonian

$$H = 2 \sum_i |i\rangle \langle i| - \sum_{\langle i,j \rangle} |i\rangle \langle j| , \tag{2.6}$$

where the second summation is over nearest neighbors $\langle i, j \rangle$. H represents the discretized version of the particle-in-a-box Hamiltonian, so we expect its ground state to be approximately a standing wave with wavelength double the box size. However, the blocking procedure just described tries to build the ground state iteratively from ground states of smaller blocks. No matter the amount of states kept, the final result will always incur large errors.

For this simple model, White and Noack solved the problem by diagonalizing the Hamiltonian of a block with different boundary conditions, and combining the lowest eigenstates of each. Additionally, they noted that diagonalizing $p > 2$ blocks, and projecting out $p - 2$ blocks to arrive at H_{AA} also gives accurate results, and that this is a generalization of applying multiple boundary conditions. In the limit $p \to \infty$ this method becomes exact, since we then find exactly the correct contribution of H_{AA} to the final ground state. It is a slightly changed version of this last method that is now known as DMRG.

2.2.3 Density matrix method

The fundamental idea of the density matrix renormalization group method rests on the fact that if we know the state of the final lattice, we can find the m most important states for H_{AA} by diagonalizing the reduced density matrix ρ_{AA} of the two blocks.

To see this, suppose, for simplicity, that the entire lattice is in a pure state[1] $|\Psi\rangle = \sum c_{b,e} |b\rangle |e\rangle$, with $b = 1, \ldots, l$ the states of H_{AA} and $e = 1, \ldots, N_{\text{env}}$ the environment states. The reduced density matrix is given by

$$\rho_{AA} = \sum_e |\Psi\rangle \langle\Psi| = \sum_{b,b'} c_{b,e} c_{b',e} |b\rangle \langle b'| \tag{2.7}$$

We now wish to find a set of orthonormal states $|\lambda\rangle \in \mathcal{H}_{AA}$, $\lambda = 1, \ldots, m$ with $m < l$, such that the quadratic norm

$$\| |\Psi\rangle - |\widetilde{\Psi}\rangle \| = 1 - 2 \sum_{\lambda,b,e} a_{\lambda,e} c_{b,e} u_{\lambda,b} + \sum_{\lambda,e} a_{\lambda,e}^2 \tag{2.8}$$

is minimized. Here,

$$|\widetilde{\Psi}\rangle = \sum_{\lambda=1}^{m} \sum_{e=1}^{N_{\text{env}}} a_{\lambda,e} |\lambda\rangle |e\rangle \tag{2.9}$$

is the representation of $|\Psi\rangle$ given the constraint that we can only use m states from $\mathcal{H}_{AA}$. The $u_{\lambda,b}$ are given by

$$\lambda = \sum_b u_{\lambda,b} |b\rangle . \tag{2.10}$$

We need to minimize Eq. 2.8 with respect to $a_{\lambda,e}$ and $u_{\lambda,b}$. Setting the derivative with respect to $a_{\lambda,e}$ equal to 0 yields

$$-2 \sum_{\lambda,b,e} c_{b,e} u_{\lambda,b} + 2 \sum_{\lambda,e} a_{\lambda,e} = 0 \tag{2.11}$$

So we see that $a_{\lambda,e} = \sum_b c_{b,e} u_{\lambda,b}$, and we are left to minimize

$$1 - \sum_{\lambda,b,b'} u_{\lambda,b} (\rho_{AA})_{b,b'} u_{\lambda,b'} \tag{2.12}$$

with respect to $u_{\lambda,b}$. But this is equal to

$$1 - \sum_{\lambda=1}^{m} \langle\lambda| \rho_{AA} |\lambda\rangle \tag{2.13}$$

[1] For a proof for a mixed state, see [34]

and because the eigenvalues of ρ_{AA} represent probabilities and are thus non-negative, this is clearly minimal when $|\lambda\rangle$ are the m eigenvectors of ρ_{AA} corresponding to the largest eigenvalues. This minimal value is

$$1 - \sum_{\lambda=1}^{m} w_\lambda \tag{2.14}$$

with w_λ the eigenvalues of the reduced density matrix.

Eq. 2.14 is called the truncation error or residual probability, and quantifies the incurred error when taking a number $m < l$ states to represent $\mathcal{H}_{AA}$.

We have proven that the optimal (in the sense that $\| |\Psi\rangle - |\widetilde{\Psi}\rangle \|$ is minimized[2]) states to keep for a subsystem are the states given by the reduced density matrix, obtained by tracing out the entire lattice in the ground state (or some other target state). The problem, of course, is that we do not know the state of the entire lattice, since that is exactly what we're trying to approximate.

Instead then, we should try to calculate the reduced density matrix of the system embedded in *some* larger environment, as closely as possible resembling the one in which it should be embedded. The combination of the system block and this environment block is usually called *superblock*. Analogous to how White and Noack solved the particle in a box problem, we could calculate the ground state of $p > 2$ blocks, and trace out all but 2, doubling our block size each iteration. In practice, this does not work well for interacting Hamiltonians, since this would involve finding the largest eigenvalue of a $N^p_{\text{block}} \times N^p_{\text{block}}$ matrix (compare this with the particle in a box Hamiltonian, which only grows linearly in the amount of lattice sites).

The widely adopted algorithm proposed by White [36] for finding the ground state of a system in the thermodynamic limit proceeds as follows.

2.2.4 Infinite-system method

Instead of using an exponential blocking procedure (doubling or tripling the amount of effective sites in a block at each iteration), the infinite-system method in the DMRG formulation adds a single site before truncating the Hilbert space to have at most m basis states.

[2] There are several other arguments for why these states are optimal, for example, they minimize the error in expectation values $\langle A \rangle$ of operators. For an overview, see [35].

1. Consider a block A of size l, with l small. Suppose, for simplicity, that the number of basis states of the block is already m. States of this block can be written as

$$|\Psi_A\rangle = \sum_{b=1}^{m} c_i \, |b\rangle \, . \tag{2.15}$$

   The Hamiltonian is written as (similarly for other operators):

$$\hat{H}_A = \sum_{b,b'}^{m} H_{bb'} \, |b\rangle \, \langle b| \, . \tag{2.16}$$

2. Construct an enlarged block with one additional site, denoted by $A\cdot$. States are now written

$$|\Psi_{A\cdot}\rangle = \sum_{b,\sigma} c_{b,\sigma} \, |b\rangle \otimes |\sigma\rangle \, . \tag{2.17}$$

   Here, σ runs over the d local basis states of $\mathscr{H}_{\text{site}}$.

3. Construct a superblock, consisting of the enlarged system block $A\cdot$ and a reflected environment block $\cdot A$, together denoted by $A\cdot\cdot A$. Find the ground state $|\Psi_0\rangle$ of $A\cdot\cdot A$, for example with the Lanczos method [37].

4. Obtain the reduced density matrix of the enlarged block by tracing out the environment, and write it in diagonal form.

$$\begin{aligned} \rho_{A\cdot} &= \sum_{e,\sigma} (\langle\sigma| \otimes \langle e|) \, |\Psi_0\rangle \, \langle\Psi_0| \, (|\sigma\rangle \otimes |e\rangle), \\ &= \sum_{i=1}^{dm} w_i \, |\lambda_i\rangle \, \langle\lambda_i| \, . \end{aligned} \tag{2.18}$$

   Here, we have chosen $w_0 >= w_1 \ldots >= w_{dm}$. In this basis, the Hamiltonian is written as

$$\hat{H}_{A\cdot} = \sum_{i,j}^{dm} H_{ij} \, |\lambda_i\rangle \, \langle\lambda_j| \, . \tag{2.19}$$

5. Truncate the Hilbert space by keeping only the m eigenstates of $\rho_{A\cdot}$ with largest eigenvalues. Operators truncate as follows:

$$\widetilde{\rho}_{A\cdot} = \sum_{i=1}^{m} w_i \left|\lambda_i\right\rangle \left\langle\lambda_j\right|, \tag{2.20}$$

$$\widetilde{H}_{A\cdot} = \sum_{i,j}^{m} H_{ij} \left|\lambda_i\right\rangle \left\langle\lambda_j\right|. \tag{2.21}$$

6. Set $H_A \leftarrow \widetilde{H}_{A\cdot}$ and return to 1.

This method finds ground state energies in the thermodynamic limit with astounding accuracy, and has been the reference point in all 1D quantum lattice simulation since its invention.

3

DRMG applied to two-dimensional classical lattice models

This chapter explains how to apply the ideas of the density matrix renormalization group to two-dimensional classical lattices.

First, we explain the transfer-matrix formulation for classical partition functions. Then, we show how to renormalize the transfer matrix using DMRG. This was first done by Nishino [38]. To make notation easier and up-to-date with current approaches, we redefine the transfer matrix in terms of a tensor network. Then, we explain the corner transfer matrix renormalization group (CTMRG) method. This method, first introduced by Nishino and Okunishi [4], unifies ideas from Baxter [1, 2, 19] and White [5] to significantly speed up the renormalization of the transfer matrix.

Finally, we show how to compute various quantities with the CTMRG method and make some remarks about the spectrum of the corner transfer matrix.

3.1 Statistical mechanics on classical lattices

For a general introduction to statistical mechanics, we refer to [39].

The central quantity in equilibrium statistical mechanics is the partition function Z, which, for a discrete system such as a lattice, is defined as

$$Z = \sum_s \exp\left(-\beta H(s)\right), \tag{3.1}$$

where the sum is over all microstates s, H is the energy function, and $\beta = T^{-1}$ the inverse temperature.

The probability that the system is in a particular microstate

$$p(s) = \frac{\exp(-\beta H(s))}{Z} \tag{3.2}$$

is also called the *Boltzmann weight*.

At first glance, the partition function is a simple normalization factor. But its importance stems from the fact that since it contains all statistical information about the system, all thermodynamic quantities can be expressed as a function of Z.

The energy of the system is expressed as

$$\langle E \rangle = \frac{\sum_s H(s) \exp(-\beta H(s))}{Z} = -\frac{\partial}{\partial \beta} \log Z, \tag{3.3}$$

the entropy as

$$S = -\sum_s p(s) \log p(s) = \frac{\partial}{\partial T}(T \log Z), \tag{3.4}$$

and the free energy as

$$F = \langle E \rangle - TS = T^2 \frac{\partial}{\partial T} \log Z - T \frac{\partial}{\partial T}(T \log Z) = -T \log Z. \tag{3.5}$$

3.2 Transfer matrices of lattice models

Transfer matrices are used to re-express the partition function of classical lattice systems, allowing them to be solved exactly or approximated.

We will introduce the transfer matrix in the context of the 1D classical Ising model, first introduced and solved using the transfer matrix method by Ising [40] in his PhD thesis.

3.2.1 1D Ising model

Consider the 1D ferromagnetic Ising model [40], defined by the energy function

$$H(\sigma) = -J \sum_{\langle ij \rangle} \sigma_i \sigma_j - h \sum_i \sigma_i. \tag{3.6}$$

Here, we sum over nearest neighbors $\langle ij \rangle$ and the spins σ_i take the values ± 1. $J > 0$ is the spin coupling and $h > 0$ an external magnetic field.

Assume, for the moment, that the chain consists of N spins, and apply periodic boundary conditions. The partition function of this system is given by

$$Z_N = \sum_{\sigma_1,\ldots,\sigma_N \in \{-1,1\}} \exp(-\beta H(\sigma)) \tag{3.7}$$

Exploiting the local nature of the interaction between spins, we can write

$$Z_N = \sum_{\sigma_1,\cdots,\sigma_N \in \{-1,1\}} \prod_{\langle i,j \rangle} e^{K\sigma_i\sigma_j + \frac{H}{2}(\sigma_i+\sigma_j)} \tag{3.8}$$

where we defined $K \equiv \beta J$ and $H \equiv \beta h$.

Now, we define the 2×2 matrix

$$T_{\sigma\sigma'} = \exp(K\sigma\sigma' + \frac{H}{2}(\sigma + \sigma')). \tag{3.9}$$

for which a possible choice of basis is

$$(|\uparrow\rangle = 1, |\downarrow\rangle = -1) = (\begin{bmatrix}1\\0\end{bmatrix}, \begin{bmatrix}0\\1\end{bmatrix}). \tag{3.10}$$

In terms of this matrix, Z_N is written as

$$Z_N = \sum_{\sigma_1,\cdots,\sigma_N} T_{\sigma_1\sigma_2}\cdots T_{\sigma_N\sigma_1} = \mathrm{Tr}\, T^N. \tag{3.11}$$

T is called the transfer matrix. In the basis of Eq. 3.10, it is written as

$$T = \begin{bmatrix} e^{K+H} & e^{-K} \\ e^{-K} & e^{K-H} \end{bmatrix}. \tag{3.12}$$

T is, in fact, diagonalizable. So, we can write $T^N = PD^NP^{-1}$, where P consists of the eigenvectors of T, and D has the corresponding eigenvalues on the diagonal. By the cyclic property of the trace, we have

$$Z_N = \lambda_+^N + \lambda_-^N, \tag{3.13}$$

where

$$\lambda_\pm = e^K \left[\cosh(H) \pm \sqrt{\sinh^2(H) + e^{-4K}}\right] \tag{3.14}$$

Thus, we have reduced the problem of finding the partition function to an eigenvalue problem.

In the thermodynamic limit $N \to \infty$

$$Z = \lim_{N\to\infty} \lambda_+^N \tag{3.15}$$

where λ_+ is the non-degenerate largest eigenvalue (in absolute value) of T. Thermodynamic quantities like the free energy per site

$$\frac{F}{N} = -T \log \lambda_+ \tag{3.16}$$

and the magnetization per site

$$M = \frac{\sum_i^N \langle \sigma_i \rangle}{N} = -\frac{1}{N}\frac{\partial F}{\partial h} \tag{3.17}$$

can now readily be calculated.

3.2.1.1 Fixed boundary conditions

We may also apply fixed boundary conditions. The partition function is then written as

$$Z_N = \langle \sigma' | \, T^N \, | \sigma \rangle \,, \tag{3.18}$$

where $|\sigma\rangle$ and $|\sigma'\rangle$ are the right and left boundary spins.

In the large-N limit, T^N tends towards the projector onto the eigenspace spanned by the eigenvector belonging to the largest eigenvalue

$$|\lambda_+\rangle = \lim_{N\to\infty} \frac{T^N \, |\sigma\rangle}{\left\| T^N \, |\sigma\rangle \right\|}. \tag{3.19}$$

Eq. 3.19 is true for any $|\sigma\rangle$ that is not orthogonal to $|\lambda_+\rangle$.

The physical significance of the normalized lowest-lying eigenvector $|\lambda_1\rangle$ is that $\langle \lambda_1 | \uparrow \rangle$ and $\langle \lambda_1 | \downarrow \rangle$ represent the Boltzmann weight of $|\uparrow\rangle$ and $|\downarrow\rangle$ at the boundary of a half-infinite chain.

3.2.2 2D Ising model

Next, we treat the two-dimensional, square-lattice Ising model, which was solved in 1944 by Onsager [11] in a groundbreaking effort[1]. The energy function is still written as in Eq. 3.6, but now every lattice site has four neighbors.

Let N be the number of columns and l be the number of rows of the lattice, and assume $l \gg N$. In the vertical direction, we apply periodic boundary conditions, as in the one-dimensional case. In the horizontal direction, we keep an open boundary. We refer to N as the system size.

Similarly as in the 1D case, the partition function can be written as

$$Z_N = \sum_{\boldsymbol{\sigma}} \prod_{\langle i,j,k,l \rangle} W(\sigma_i, \sigma_j, \sigma_k, \sigma_l) \tag{3.20}$$

where the product runs over all groups of four spins sharing the same face. The Boltzmann weight of such a face is given by

$$W(\sigma_i, \sigma_j, \sigma_k, \sigma_l) = \exp\left\{\frac{K}{2}(\sigma_i\sigma_j + \sigma_j\sigma_k + \sigma_k\sigma_l + \sigma_l\sigma_i)\right\} \tag{3.21}$$

We can express the Boltzmann weight of a configuration of the whole lattice as a product of the Boltzmann weights of the rows

$$Z_N = \sum_{\boldsymbol{\sigma}} \prod_{r=1}^{l} W(\sigma_1^r, \sigma_2^r, \sigma_1^{r+1}, \sigma_2^{r+1}) \ldots W(\sigma_{N-1}^r, \sigma_N^r, \sigma_{N-1}^{r+1}, \sigma_N^{r+1}) \tag{3.22}$$

where σ_i^r denotes the value of the ith spin of row r.

Now, we can generalize the definition of the transfer matrix to two dimensions, by defining it as the Boltzmann weight of an entire row

$$T_N(\boldsymbol{\sigma}, \boldsymbol{\sigma'}) = W(\sigma_1, \sigma_2, \sigma_1', \sigma_2') \ldots W(\sigma_{N-1}, \sigma_N, \sigma_{N-1}', \sigma_N') \tag{3.23}$$

If we take the spin configurations of an entire row as basis vectors, T_N can be written as a matrix of dimensions $2^N \times 2^N$.

[1] Onsager's solution rigorously showed, for the first time, that phase transitions could appear in simple statistical models and remained for a long time the only exactly solved model exhibiting critical behaviour. For a historical overview, see [41].

Similarly as in the one-dimensional case, the partition function now becomes

$$Z_N = \sum_{\boldsymbol{\sigma}} \prod_{r=1}^{l} T_N(\boldsymbol{\sigma}^r, \boldsymbol{\sigma}^{r+1}) = \mathrm{Tr}\, T_N^l \tag{3.24}$$

In the limit of an $N \times \infty$ cylinder, the partition function is once again determined by the largest eigenvalue[2].

$$Z_N = \lim_{l\to\infty} T_N^l = \lim_{l\to\infty} (\lambda_0)_N^l \tag{3.25}$$

The partition function in the thermodynamic limit is given by

$$Z = \lim_{N\to\infty} Z_N \tag{3.26}$$

3.3 Partition function of the 2D Ising model as a tensor network

In calculating the partition function of 1D and 2D lattices, matrices of Boltzmann weights like W and T play a crucial role. We have formulated them in a way that is valid for any interaction-round-a-face (IRF) model, defined by

$$H \propto \sum_{\langle i,j,k,l\rangle} W(\sigma_i, \sigma_j, \sigma_k, \sigma_l), \tag{3.27}$$

where the summation is over all spins sharing a face. W can contain 4-spin, 3-spin, 2-spin and 1-spin interaction terms. The Ising model is a special case of the IRF model, with W given by Eq. 3.21.

We will now express the partition function of the 2D Ising model as a tensor network. The transfer matrix T is redefined in the process. This allows us to visualize the equations in a way that is consistent with the many other tensor network algorithms under research today. For an introduction to tensor network notation, see Appendix B.

[2] As in the 1D case, T is symmetric, so it is orthogonally diagonalizable.

3.3.1 Tensor network of the partition function of a system of four spins

We define

$$Q(\sigma_i, \sigma_j) = \exp(K\sigma_i\sigma_j) \tag{3.28}$$

as the Boltzmann weight of the bond between σ_i and σ_j. It is the same as the 1D transfer matrix in Eq. 3.9.

The Boltzmann weight of a face W decomposes into a product of Boltzmann weights of bonds

$$W(\sigma_i, \sigma_j, \sigma_k, \sigma_l) = Q(\sigma_i, \sigma_j)Q(\sigma_j, \sigma_l)Q(\sigma_l, \sigma_k)Q(\sigma_k, \sigma_i). \tag{3.29}$$

It is now easy to see that the partition function is equal to the contracted tensor network in Fig. 3.1:

$$\begin{aligned} Z_{2\times 2} &= \sum_{\sigma_1,\sigma_2,\sigma_3,\sigma_4} \sum_{a,b,c,d} \delta_{\sigma_1,a}Q(a,b)\delta_{\sigma_2,b}Q(b,c)\delta_{\sigma_3,c}Q(c,d)\delta_{\sigma_4,d}Q(d,a) \\ &= \sum_{\sigma_1,\sigma_2,\sigma_3,\sigma_4} W(\sigma_1,\sigma_2,\sigma_3,\sigma_4). \end{aligned} \tag{3.30}$$

where the Kronecker delta is defined as usual:

$$\delta_{ij} = \begin{cases} 1 & \text{if } i = j \\ 0 & \text{if } i \neq j. \end{cases} \tag{3.31}$$

3.3.2 Thermodynamic limit

We define the matrix P by

$$P^2 = Q. \tag{3.32}$$

as in Fig. 3.2. This allows us to write the partition function of an arbitrary $N \times l$ square lattice as a tensor network of a single recurrent tensor a_{ijkl}, given by

$$a_{ijkl} = \sum_{a,b,c,d} \delta_{abcd}P_{ia}P_{jb}P_{kc}P_{ld}, \tag{3.33}$$

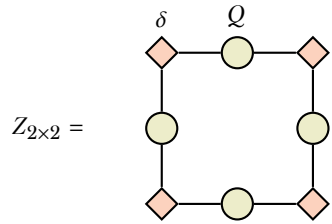

Figure 3.1: A tensor network representation of the partition function of the Ising model on a 2×2 lattice. See Eq. 3.30.

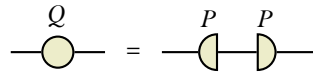

Figure 3.2: Graphical form of Eq. 3.32.

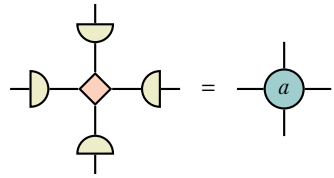

Figure 3.3: Graphical form of Eq. 3.33.

where the generalization of the Kronecker delta is defined as

$$\delta_{i_1 \ldots i_n} = \begin{cases} 1 & \text{if } i_1 = \ldots = i_n \\ 0 & \text{otherwise.} \end{cases} \tag{3.34}$$

See Fig. 3.3 and Fig. 3.4. At the edges and corners, we define suitable tensors of rank 3 and 2, which we will also denote by a:

$$a_{ijk} = \sum_{abc} \delta_{abc} P_{ia} P_{jb} P_{kc},$$
$$a_{ij} = \sum_{ab} \delta_{ab} P_{ia} P_{jb}.$$

The challenge is to approximate this tensor network in the thermodynamic limit.

3.3.3 The transfer matrix as a tensor network

With our newfound representation of the partition function as a tensor network, we can redefine the row-to-row transfer matrix from Eq. 3.23 as the tensor network expressed in Fig. 3.5. For all l, it is still true that

$$Z_{N \times l} = \operatorname{Tr} T_N^l = \sum_{i=1}^{2^N} \lambda_i^l, \tag{3.35}$$

so the eigenvalues must be the same. That means that the new definition of the transfer matrix is related to the old one by a basis transformation

$$T_{\text{new}} = P T_{\text{old}} P^T. \tag{3.36}$$

3.4 Transfer matrix renormalization group

There is a deep connection between quantum mechanical lattice systems in d dimensions and classical lattice systems in $d+1$ dimensions. Via the imaginary time path integral formulation, the partition function of a one-dimensional quantum system can be written as the partition function of an effective two-dimensional classical system. The ground state of the quantum system corresponds to the largest eigenvector of the transfer matrix of this corresponding classical system.

For more on the quantum-classical correspondence, see Appendix A.

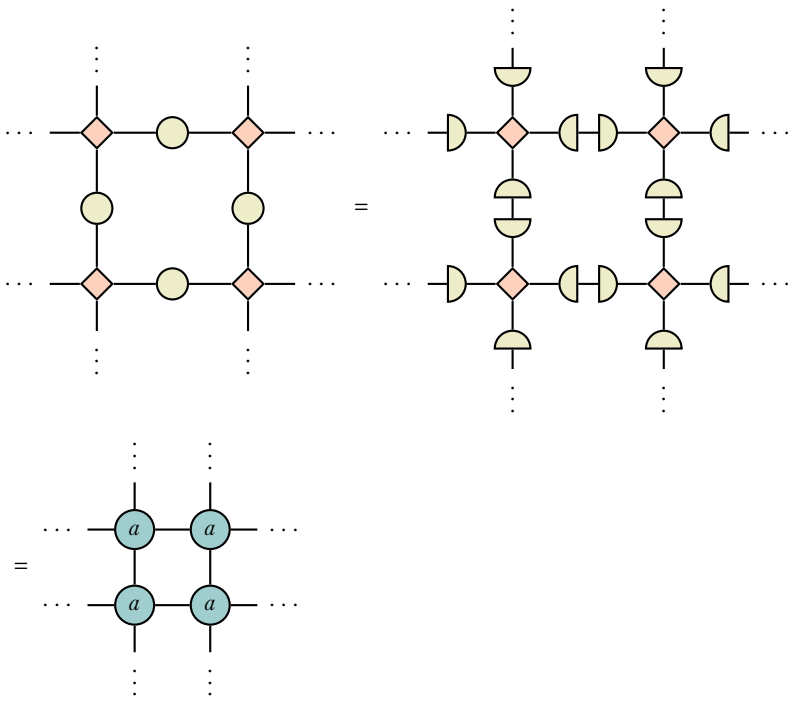

Figure 3.4: $Z_{N\times l}$ can be written as a contracted tensor network of $N \times l$ copies of the tensor a.

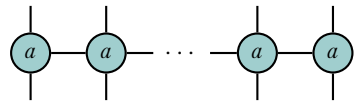

Figure 3.5: The definition of T_N as a network of N copies of the tensor a.

3.4.1 The infinite system algorithm for the transfer matrix

Nishino [4, 38] was the first to apply density matrix renormalization group methods in the context of two-dimensional classical lattices.

Analogous to the infinite system DMRG algorithm for approximating the Hamiltonian of quantum spin chains, our goal is to approximate the transfer matrix in the thermodynamic limit as well as possible within a restriced number of basis states m. We will do this by adding a single site at a time, and truncating the dimension from $2m$ to m at each iteration.

For simplicity, we assume that, at the start of the algorithm, the transfer matrix already has dimension m. We call this transfer matrix P_N.

We note that this initial P_N for a system with a free boundary can be obtained by contracting a-tensors, until P_N becomes of size $m \times m$. See Fig. 3.6.

To specify fixed instead of open boundary conditions, we may use as boundary tensor a slightly modified version of the three-legged version of a, namely

$$a^{\sigma}_{ijk} = \sum_{abc} \delta_{\sigma abc} P_{ia} P_{jb} P_{kc}, \tag{3.37}$$

that represents an edge site with spin fixed at σ.

We enlarge the system with one site by contracting with an additional a-tensor, obtaining P_{N+1}. See the first network in Fig. 3.7.

In order to find the best projection from $2m$ basis states back to m, we embed the system in an environment that is the mirror image of the system we presently have. We call this matrix T_{2N+2}. It represents the transfer matrix of $2N+2$ sites. We find the largest eigenvalue and corresponding eigenvector, as shown in Fig. 3.8.

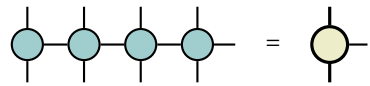

Figure 3.6: A good starting point for the half-row transfer P_N is obtained by contracting a couple of a-tensors, until P_N reaches dimension m.

The equivalent of the *reduced density matrix of a block* in the classical case is:

$$\rho_{N+1} = \sum_{\sigma_B} \langle \sigma_B | \lambda_0 \rangle \langle \lambda_0 | \sigma_B \rangle , \tag{3.38}$$

where we have summed over all the degrees of freedom of one of the half-row transfer matrices P_{N+1}. See the first step of Fig. 3.9.

The optimal renormalization

$$\widetilde{P}_{N+1} = O P_{N+1} O^\dagger \tag{3.39}$$

is obtained by diagonalizing ρ_{N+1} and keeping the eigenvectors corresponding to the m largest eigenvalues. See the second step of Fig. 3.9.

With this blocking procedure, we can successively find

$$P_{N+1} \to P_{N+2} \to \ldots , \tag{3.40}$$

until we have reached some termination condition.[3]

3.4.2 Physical interpretation of the reduced density matrix

Generalizing the remarks from section 3.2.1.1 to the two-dimensional case, we see that the normalized lowest-lying eigenvector of the transfer matrix T_N contains the Boltzmann weights of spin configurations on the boundary of a half-infinite $N \times \infty$ lattice.

Therefore, the classical equivalent of the quantum mechanical reduced density matrix, given by Eq. 3.38, and by the first network in Fig. 3.9, represents the Boltzmann weights of configurations along a cut in an $N \times \infty$ lattice.

Nishino and Okunishi [4], drawing on ideas from Baxter, realized the Boltzmann weights of configurations along this cut could be obtained by employing *corner transfer matrices*, making it unneccessary to solve the eigenvalue

[3] The termination condition for the infinite-system algorithm is discussed in section 6.3.

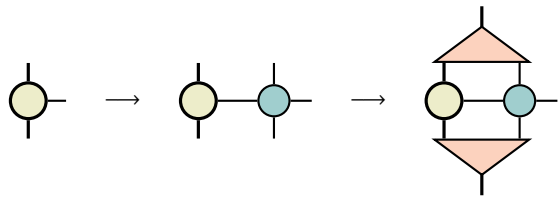

Figure 3.7: In the first step, P_{N+1} is obtained by contracting the current half-row transfer matrix P_N with an additional a-tensor. In the second step, P_{N+1} is truncated back to an m-dimensional matrix, with the optimal low-rank approximation given by keeping the basis states corresponding to the m largest eigenvalues of the density matrix. See Fig. 3.9.

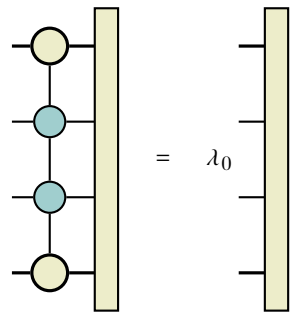

Figure 3.8: Equation for the lowest-lying eigenvector of the row-to-row transfer matrix T_{2N+2}.

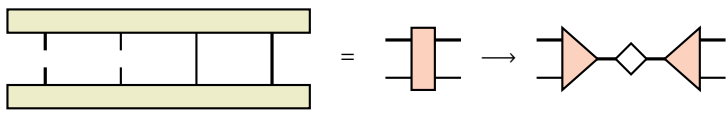

Figure 3.9: Graphical form of Eq. 3.38. In the second step, ρ_{N+1} is diagonalized and only the eigenvectors corresponding to the m largest eigenvalues are kept.

problem in Fig. 3.8. Their method, called the Corner Transfer Matrix Renormalization Group method, consumes far less resources while maintaining precision. For this reason, it is the method of choice for most of the simulations in this thesis.

3.5 Corner transfer matrix renormalization group

3.5.1 Corner transfer matrices

The concept of corner transfer matrices for 2D lattices was first introduced by Baxter [1, 2, 19]. Whereas the row-to-row transfer matrix Eq. 3.23 corresponds to adding a row to the lattice, the corner transfer matrix adds a quadrant of spins. It was originally defined by Baxter as

$$A_{\boldsymbol{\sigma},\boldsymbol{\sigma}'} = \begin{cases} \sum \prod_{\langle i,j,k,l\rangle} W(\sigma_i, \sigma_j, \sigma_k, \sigma_l) & \text{if } \sigma_1 = \sigma_1' \\ 0 & \text{if } \sigma_1 \neq \sigma_1'. \end{cases} \tag{3.41}$$

Here, the product runs over groups of four spins that share the same face, and the sum is over all spins in the interior of the quadrant.

In a symmetric and isotropic model such as the Ising model, we have

$$W(a,b,c,d) = W(b,a,d,c) = W(c,a,d,b) = W(d,c,b,a) \tag{3.42}$$

and the partition of an $N \times N$ lattice is expressed as

$$Z_{N\times N} = \operatorname{Tr} A^4 = \sum_{\alpha=1}^{2^N} \nu_\alpha^4, \tag{3.43}$$

where ν_α are the eigenvalues of A.

In the thermodynamic limit, this partition function is equal to the partition function of an $N \times \infty$ lattice, given by Eq. 3.24.

3.5.2 Corner transfer matrix as a tensor network

Similarly to how we redefined the row-to-row transfer matrix (Eq. 3.23) as the tensor network in Fig. 3.5, we can redefine the corner transfer matrix (Eq. 3.41) as the tensor network in Fig. 3.10. Again, the new and old definitions of A are related by a basis tranformation

$$A_{\text{new}} = P A_{\text{old}} P^T. \tag{3.44}$$

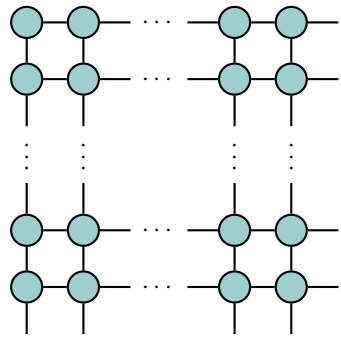

Figure 3.10: Corner transfer matrix expressed as a contraction of a-tensors.

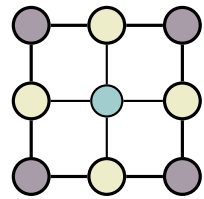

Figure 3.11: Tensor network approximation to $Z_{N\times N}$ in the CTMRG method.

The partition function, as in Eq. 3.43, is given by the tensor network in Fig. 3.11.

3.5.3 Corner transfer matrix renormalization group method

The corner transfer matrix renormalization group iteratively adds a layer to A, while keeping only m basis states at each step. It was first employed by Baxter [1, 2].

As can be seen from Eq. 3.43, the best approximation to the partition func-

tion within a restricted number of basis states m is obtained by keeping the eigenvectors corresponding to the m largest eigenvalues of A^4.

The algorithm proceeds very much like the transfer matrix renormalization group method. In addition to renormalizing the half-row transfer matrix P, we also renormalize the corner transfer matrix A at each step, using the projector obtained from diagonalizing A^4 or equivalently A.

We first initialize P_N and A_N. A free or fixed boundary may be imposed in the same way as in the transfer matrix renormalization group. See Eq. 3.37.

We then obtain the unrenormalized A_{N+1} by adding a layer of spins to the quadrant represented by A_N. This is done by contracting with two half-row transfer matrices P_N and a single a-tensor, as shown in the first step of Fig. 3.12. We obtain the unnormalized P_{N+1} as before, as shown in the first step of Fig. 3.7.

We use the projector to obtain the renormalized versions of A_{N+1} and T_{N+1}

$$\widetilde{A}_{N+1} = OA_{N+1}O^\dagger, \tag{3.45}$$

$$\widetilde{T}_{N+1} = OT_{N+1}O^\dagger. \tag{3.46}$$

shown in the second steps of Fig. 3.12 and Fig. 3.7.

We repeat the above procedure to successively obtain

$$A_{N+1} \to A_{N+2} \to \ldots, \tag{3.47}$$

$$T_{N+1} \to T_{N+2} \to \ldots \tag{3.48}$$

until a convergence criterion is reached.

3.5.3.1 Equivalence to TMRG and DMRG in the thermodynamic limit

A^4 contains the Boltzmann weights of spins along a cut in the middle of the $N \times N$ system. In contrast, the matrix in Eq. 3.38 contains the Boltzmann weights of spins along a cut down the middle of an $N \times \infty$ system.

In the thermodynamic limit, both become the same, and we can make the identification

$$\rho = A^4. \tag{3.49}$$

See Fig. 3.13.

Hence, DMRG and TMRG are equivalent to CTMRG in the thermodynamic limit. This was first realized by Nishino [42].

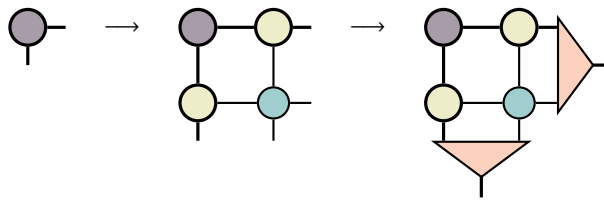

Figure 3.12: In the first step, the unrenormalized A_{N+1} is obtained by contracting with two copies of P_N and a single a-tensor. This corresponds to adding a layer of spins to the quadrant, thus enlarging it from $N \times N$ to $N+1 \times N+1$. In the second step, A_{N+1} is renormalized with the projector obtained from diagonalizing A^4_{N+1} and keeping the basis states corresponding to the m largest eigenvalues.

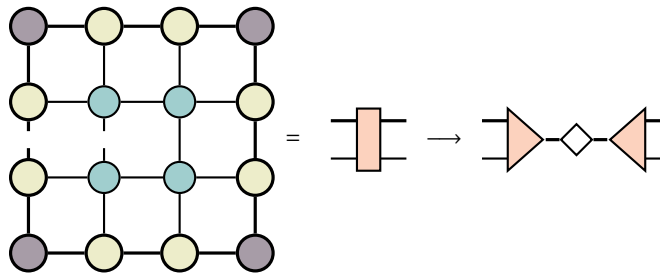

Figure 3.13: The matrix A^4_{N+1} is approximately equal to ρ_{N+1} in Eq. 3.38. Compare the graphical forms of this network and the one shown in Fig. 3.9. We obtain the optimal projector by diagonalizing A^4_{N+1}, or equivalently A_{N+1}.

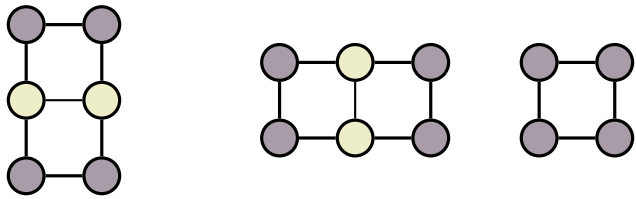

Figure 3.14: From left to right: r_2, r_3 and r_4 as in Eq. 3.51.

3.6 Calculation of observable quantities

3.6.1 Free energy per site

Baxter [1, 2] showed that the partition function per site

$$\kappa = Z^{1/N^2} \tag{3.50}$$

is, within the corner transfer matrix renormalization group method, written as

$$\kappa = \frac{r_1 r_4}{r_2 r_3}, \tag{3.51}$$

with r_2, r_3 and r_4 as in Fig. 3.14 and $r_1 = Z_{N\times N}$ as in Fig. 3.11. The free energy per site is then simply

$$\frac{F}{N^2} = -T \log \kappa. \tag{3.52}$$

3.6.2 Magnetization per site

The magnetization per site may be calculated as

$$M = T \frac{\partial(\log \kappa)}{\partial h}, \tag{3.53}$$

but this involves a numerical derivative and a numerical limit $h \to 0$ in the case of the spontaneous magnetization. A more practical method, that is employed in this thesis, is to use the magnetization of the central spin

$$\langle \sigma_0 \rangle = \frac{\sum_{\{\boldsymbol{\sigma}\}} \sigma_0 \exp\left(-\beta H(\boldsymbol{\sigma})\right)}{Z} \tag{3.54}$$

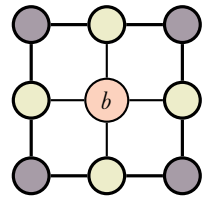

Figure 3.15: Unnormalized expectation value of central spin, with the tensor b_{ijkl} defined in Eq. 3.56.

as a proxy quantity to the magnetization per site.

In the original definition of the corner transfer matrix by Baxter (Eq. 3.41), it is written as

$$\langle \sigma_0 \rangle = \frac{\mathrm{Tr} A_+^4 - \mathrm{Tr} A_-^4}{\mathrm{Tr} A^4}. \tag{3.55}$$

Here, $A_\pm$ is the corner transfer matrix with the central spin fixed to $\pm$.

In tensor network notation, $\mathrm{Tr} A_+^4 - \mathrm{Tr} A_-^4$ is written as the tensor network in Fig. 3.15, with the tensor b_{ijkl} defined as

$$b_{ijkl} = \sum_{\sigma \in \{-1,1\}} \sigma \delta_{\sigma ijkl}. \tag{3.56}$$

All numerical results in this thesis involving the magnetization per site are actually obtained by calculating $\langle \sigma_0 \rangle$, which shall be referred to simply as M from now on.

3.6.3 Analogy to entanglement entropy for classical systems

The key point of the corner transfer matrix renormalization group method [4, 42] is that it unifies White's density matrix renormalization group method [5] with Baxter's corner transfer matrix approach [1, 19], through the identification (in the isotropic case)

$$\rho_{\text{half-chain}} = A^4. \tag{3.57}$$

This allows one to define a 2D classical analogue to the half-chain entanglement entropy of a 1D quantum system

$$S_{\text{classical}} = -\operatorname{Tr} A^4 \log A^4 = -\sum_{\alpha=1}^{m} \nu_\alpha^4 \log \nu_\alpha^4, \tag{3.58}$$

where ν_α are the eigenvalues of the corner transfer matrix A. In the CTMRG algorithm, A is kept in diagonal form, making $S_{\text{classical}}$ trivial to compute.

In [43], numerical evidence is given for the validity of Eq. 3.58 for a wide range of models, and the concept is generalized to higher dimensions. For an overview of applying corner transfer matrices in higher dimensions and to quantum systems, see [44].

3.7 Spectrum of the corner transfer matrix

3.7.1 Analytical results for the Ising model

In what follows, we present results established in [45, 46].

For the off-critical Ising model on a square lattice, we have [47]

$$\hat{\rho} = \hat{A}^4 = \exp(-\hat{H}_{\text{CTM}}), \tag{3.59}$$

where

$$\hat{H}_{\text{CTM}} = \sum_{l=0}^{\infty} \epsilon_l(T) c_l^\dagger c_l, \tag{3.60}$$

with c_l and $c_l^\dagger$ fermionic annihilation and creation operators and

$$\epsilon_l = \begin{cases} (2l+1)\epsilon(T) & \text{if } T > T_c, \\ 2l\epsilon(T) & \text{if } T < T_c. \end{cases} \tag{3.61}$$

with $\epsilon(T)$ a model-specific factor that only depends on temperature.

In other words, the reduced density matrix (or equivalently, the corner transfer matrix A) can be written as a density matrix of an effective free fermionic Hamiltonian with equally spaced excitations.

What does this mean for the spectrum of A? If we assume a free boundary, we have to distinguish between the ordered and disordered phase.

In the disordered phase, we have $\epsilon_l = (2l+1)\epsilon(T)$. The ground state, $E = 0$, corresponds to the vacuum state of the effective system described by

H_{CTM}. The single-fermion excitations give ϵ, 3ϵ, 5ϵ, ..., while two-fermion excitations give 4ϵ ($c_0^\dagger c_1^\dagger |0\rangle$), 6ϵ ($c_0^\dagger c_2^\dagger |0\rangle$) and 8ϵ ($c_0^\dagger c_3^\dagger |0\rangle$ *or* $c_1^\dagger c_2^\dagger |0\rangle$). So the first degeneracy appears at 8ϵ. 9ϵ is also degenerate: it can be constructed with a single-fermion excitation ($c_4^\dagger |0\rangle$) and a three-fermion excitation ($c_2^\dagger c_1^\dagger c_0^\dagger |0\rangle$).

The numerical results from the CTMRG algorithm exactly confirm this picture. See the $T = 2.6$ line in the left panel of Fig. 3.16. The gap after the first two eigenvalues is due to the absence of the level 2ϵ. The ϵ_l are linear and the degeneracies are correct.

In the ordered phase, we have a two-fold degeneracy for every state due to symmetry and ground state energy $E = 0$. After that, the only available levels are 2ϵ, 4ϵ, 6ϵ, ... The degeneracy of the nth energy level is given by $2p(n)$, twice the number of partitions of n into distinct integers [48], with the factor of two coming from symmetry.

To illustrate: $c_1^\dagger c_2^\dagger |0\rangle$ and $c_3^\dagger |0\rangle$ both have $E = 6\epsilon$, the third energy level (counting the vacuum as the zeroth energy level), which is to say $p(3) = 2$ since $\{3, 2 + 1\}$ are the ways to write 3. The line $T = 2$ in the left panel of Fig. 3.16 confirms these results.

With a fixed boundary, the spectrum in the disordered phase doesn't change. In the ordered phase however, the two-fold degeneracy due to symmetry is lifted, so the degeneracy of the nth energy level becomes $p(n)$. As a consequence, the spectrum decays much faster. See the right panel of Fig. 3.16.

At or close to criticality, the expression in Eq. 3.59 breaks down, and the spectrum of $\hat{\rho}$ is smoothened out. In general, below and at criticality, the spectrum decays slower for a free boundary. This is to be expected, since A preserves the symmetry when the boundary is free. At $T = 0$, A has two equally large non-zero eigenvalues, representing either all up or all down spins on the boundary of the quadrant, while for a fixed boundary, A has one non-zero eigenvalue: it represents a completely polarized state.

3.7.2 Implications for finite-m simulations

When approximating the corner transfer matrix with a free boundary in the ordered phase, it is crucial to retain all basis states corresponding to an energy level [48]. Failure to do so will lead to a symmetry-broken state.

Near criticality, however, even when all degenerate basis states are kept, the algorithm is still prone to symmetry breaking.

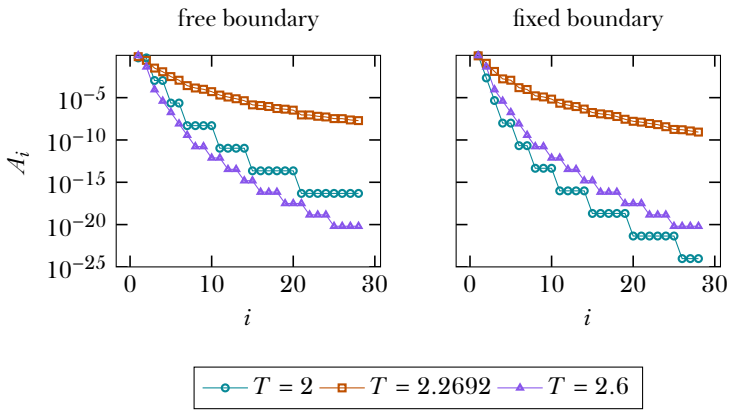

Figure 3.16: First part of the spectrum of A after $n = 1000$ steps with a bond dimension of $m = 250$.

3.8 Equivalence to variational approximation in the space of matrix product states.

In closing this chapter, we note that it has been widely established that DMRG produces a ground state that corresponds to a variational optimization within a matrix-product structure [20, 21].

CTMRG and TMRG, by the classical-quantum equivalence, find transfer matrices with similar structure. This was first noted by Baxter [2].

For an introduction to these algorithms from this variational point of view, see [49].

4
Critical behaviour and finite-size scaling

In this chapter, we introduce the central concepts in critical phenomena and finite-size scaling, largely following the review by Barber [50] and the less technical overview by Kadanoff [8].

4.1 Phase transitions

When matter exhibits a sudden change in behaviour, often characterized by a discontinuity or divergence of one or more thermodynamic quantities, we say it undergoes a *phase transition*.

A quantity that signifies this change is called an *order parameter*, which can take vastly different forms across systems and transitions. For example, for the transition of a ferromagnet, the order parameter is the net magnetization of the system, while for a percolation transition, it is the size of the largest connected graph.

For a historical account of the classification of phase transitions, see [51]. At the present time, we distinguish between two different types [8].

When some thermodynamic quantity changes discontinuously, i.e. shows a jump, we call the transition *first order*. In contrast, during a *continuous* phase transition a variable undergoes change continuously. The point at which a continuous phase transition occurs, is called the critical point.

The two-dimensional Ising model in a magnetic field shows both types of transition. At zero magnetic field and $T = T_c = 1/(\log(1 + \sqrt{2}))$, the magnetization changes from zero for $T > T_c$ to a finite value for $T < T_c$ in a continuous manner.

Below the critical temperature T_c, when the magnetic field h tends to zero from $h > 0$, the magnetization tends to a positive value. Conversely, when the magnetic field tends to zero from $h < 0$, the magnetization tends to a

negative value. Thus, across the region $h = 0, T < T_c$ the system undergoes a first-order phase transition.

4.1.1 Finite systems

We will now argue that a phase transition cannot occur in a finite system, but only happens when the number of particles tends to infinity.

Because thermodynamic quantities are averages over all possible microstates of a system, those quantities are completely defined in terms of the system's partition function, or equivalently its free energy.

Since in a finite system, the partition function is a finite sum of exponentials, it is analytic (infinitely differentiable). Hence, thermodynamic quantities cannot show true discontinuities and the phase transitions described in the above section do not occur.

4.2 Critical behaviour

We will now focus our attention on continuous phase transitions, more specifically the one that occurs in the two-dimensional Ising model. Before we discuss the behaviour of the free energy around the critical point, we briefly summarize how the thermodynamic limit is approached far away from it. Here, we largely follow [50].

We assume that the free energy per site in the thermodynamic limit

$$f_\infty(T) = \lim_{N\to\infty} \frac{F(T,N)}{N} \tag{4.1}$$

exists, and is not dependent on boundary conditions. By definition, it is not analytic in a region around the critical point.

Outside that region, however, we can write

$$F(T,N) = N f_\infty(T) + o(N), \tag{4.2}$$

where correction terms $g(N)$ of $o(N)$ (little-o of N) obey

$$\lim_{N\to\infty} \frac{g(N)}{N} = 0. \tag{4.3}$$

These corrections, of course, do depend on boundary conditions.

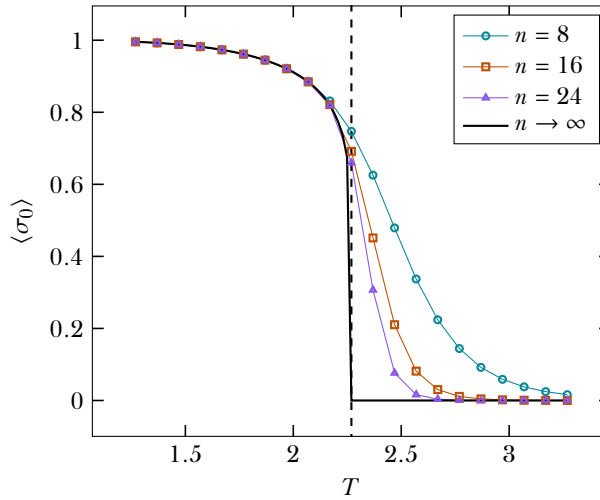

Figure 4.1: The magnetization of the central spin for small lattices with boundary spins fixed to +1. The black line is the exact solution in the thermodynamic limit.

Eq. 4.2 is valid only outside the critical region precisely because $F(T, N)$ is analytic *everywhere*, and $f_\infty(T)$ is only analytic away from the critical point.

The behaviour of $F(T, N)$ (and hence, all thermodynamic quantities) at criticality is approached is described by *finite-size scaling*.

4.2.1 Finite-size scaling

Fig. 4.1 shows the behaviour of the order parameter obtained by exact diagonalization of the partition function of small lattices. It is clear that far from the critical point, the order parameter is essentially not dependent on system size, while in critical region there are significant deviations from the thermodynamic behaviour.

One can now define two characteristic temperatures [50, 52]. The first being the cross-over temperature T_X at which finite-size effects become im-

portant, which is predicted to scale as

$$|T_X - T_c| \propto N^{-\theta}. \tag{4.4}$$

θ is called the cross-over or rounding exponent.

The second characteristic temperature is the pseudocritical temperature, denoted by $T^\star$. It can be defined in several ways, one being the point where the order parameter becomes almost zero, or the point where the heat capacity

$$C = T^2 \frac{\partial^2 F}{\partial T^2} \tag{4.5}$$

reaches its maximum. $T^\star$ can be regarded as the point where the finite system in some sense comes closest to undergoing a transition.

Generally $T^\star$ will not equal T_X. Furthermore, $T^\star$ depends on boundary conditions: periodic or fixed boundary conditions will nudge the system into an ordered state, therefore $T^\star > T_c$. Free boundary conditions will cause the system to favor disorder and the pseudocritical temperature to be lowered.

In any case, it is predicted that

$$|T^\star - T_c| \propto N^{-\lambda}. \tag{4.6}$$

It is generally accepted that [50]

$$\lambda = \theta. \tag{4.7}$$

Furthermore, if one assumes that finite-size effects become important once the correlation length of the system becomes of order of the system size, i.e. [52]

$$\xi(T_X(N)) \propto N, \tag{4.8}$$

then the correlation length exponent ν, given by

$$\xi(T) \propto |T - T_c|^{-\nu} \tag{4.9}$$

is, by using Eq. 4.4, related to θ as

$$\theta = \frac{1}{\nu}. \tag{4.10}$$

4.2.1.1 The finite-size scaling ansatz

The behaviour of a system of finite size N is expected to be a function of the ratio

$$y = \frac{N}{\xi(T)}, \tag{4.11}$$

where $\xi(T)$ is the correlation length of the thermodynamic system [53].

With the assumption in Eq. 4.8, this means that in the limit $y \gg 1$, we expect to see thermodynamic behaviour, while for $y \ll 1$, the finite system size should enter in the analysis.

To see exactly how this happens, consider as an example the order parameter M, which in the thermodynamic limit, close to the critical point obeys

$$M(T) \propto \begin{cases} (-t)^{\beta} & \text{if } T \leq T_c, \\ 0 & \text{if } T \geq T_c, \end{cases} \tag{4.12}$$

where we have defined the reduced temperature

$$t = \frac{T - T_c}{T_c}. \tag{4.13}$$

Assuming the correlation length diverges algebraically

$$\xi(T) \propto |t|^{-\nu}, \tag{4.14}$$

for $T < T_c$ we have

$$M(T) \propto \xi(T)^{-\beta/\nu}. \tag{4.15}$$

The *finite-size scaling ansatz* now says that for finite systems

$$M(T, N) = N^{-\beta/\nu} \mathcal{F}(y), \tag{4.16}$$

with the requirement that for $N \to \infty$, it should reproduce the thermodynamic behaviour in Eq. 4.15, leading to

$$\lim_{y \to \infty} \mathcal{F}(y) \propto y^{\beta/\nu}. \tag{4.17}$$

At the critical point, however, the bulk correlation length diverges and the only relevant length scale is N, so that we must have

$$M(T = T_c, N) \propto N^{-\beta/\nu}, \tag{4.18}$$

from which it follows that

$$\lim_{y \to 0} \mathcal{F}(y) = \text{const.} \tag{4.19}$$

4.2.1.2 Extracting exponents from numerical simulation

To extract critical exponents from (finite) numerical simulations, Eq. 4.16 may be written as

$$M(T, N) = N^{-\beta/\nu}\mathcal{G}(tN^{1/\nu}) \tag{4.20}$$

where it is used that (per Eq. 4.14)

$$y = \frac{N}{\xi(T)} \propto t^{\nu}N, \tag{4.21}$$

and the new scaling function is customarily written as having argument $tN^{1/\nu} = (t^{\nu}N)^{1/\nu}$.

As a side note, we mention that the most generally valid ansatz is actually

$$M(T, N) = N^{-\beta/\nu}\mathcal{G}(t^{\star}(N)N^{1/\nu}) \tag{4.22}$$

with

$$t^{\star}(N) = T - T^{\star}(N). \tag{4.23}$$

At T_c, we recover Eq. 4.18. To see this, consider that at T_c

$$t^{\star}(N) = T^{\star}(N) - T_c = aN^{-\lambda} = aN^{-1/\nu}, \tag{4.24}$$

where in the final equality we have used Eq. 4.10, so that we have

$$M(T = T_c, N) = N^{-\beta/\nu}\mathcal{G}(aN^{-1/\nu}N^{1/\nu}) \propto N^{-\beta/\nu}. \tag{4.25}$$

In this thesis, we will mostly work with Eq. 4.20, but return to Eq. 4.22 when the value of T_c is not exactly known.

The critical exponents β and ν and the critical temperature can now be extracted by asserting that the numerical data for different system sizes should collapse on a single curve

$$\mathcal{G}(tN^{1/\nu}) = M(T, N)N^{\beta/\nu}. \tag{4.26}$$

The authors of [54] propose a measure of the fitness $P(\beta, \nu, T_c)$ of such a data collapse

$$P(\beta, \nu, T_c) = \frac{1}{\mathcal{N}_{\text{overlap}}} \sum_{p} \sum_{j \neq p} \sum_{i_{\text{overlap}}} |M(t_{ij}, N_j)N_j^{\beta/\nu} - \mathcal{G}_p(t_{ij}N_j^{1/\nu})|, \tag{4.27}$$

where for each system size N_p, the data points collected for the other system sizes N_j that overlap (that is, fall between any two data points collected for N_p) are compared with the interpolation $\mathscr{E}_p(t_{ij}N_j^{1/\nu})$ between those two data points. t_{ij} is the ith temperature of the jth data point of N_j. $\mathscr{N}_{\text{overlap}}$ is the number of overlapping pairs.

It is clear that

$$P(\beta, \nu, T_c) \geq 0 \tag{4.28}$$

and the optimal values for β, ν and T_c minimize $P(\beta, \nu, T_c)$.

This measure for the data collapse is found, for data collected for this thesis, to work significantly better than other proposed measures such as fitting a polynomial or order 3-8 through all data points.

5
Finite-m scaling in the CTMRG algorithm

The connection between finite-size scaling, as introduced in the last chapter, and finite-size effects as a consequence of the finite bond dimension m within the CTMRG algorithm is made.

We discuss ideas by Nishino [7], who was the first to investigate these effects, by linking the finite-bond dimension m to the inherently finite correlation length of the approximated system at the critical point.

Then, we discuss a more recent theory of finite-entropy scaling, developed in [30] (earlier numerical evidence was given in [29, 55]), which implies a scaling of the correlation length for a matrix product state with finite bond dimension of the form $\xi \propto m^{\kappa}$.

5.1 Introduction

Up until now, we have developed our scaling analysis in terms of a finite system size N. But the approximation of the infinite-system partition function with the CTMRG algorithm depends on two parameters; the system size N and the bond dimension m.

A finite bond dimension m carries a characteristic length scale. Baxter [1], and later Östlund and Rommer [20] (in the context of one-dimensional quantum systems) showed that in the thermodynamic limit, CTMRG and DMRG are variational optimizations in the space of matrix product states.

It is known that an MPS-ansatz with finite bond dimension inherently limits the correlation length of the system to a finite value [21, 56]. Hence, thermodynamic quantities obtained from the CTMRG algorithm with finite m, in the limit $N \to \infty$, cannot diverge and must show finite-size effects similar to those of some effective finite system of size $N_{\mathrm{eff}}(m)$ depending on the bond dimension m.

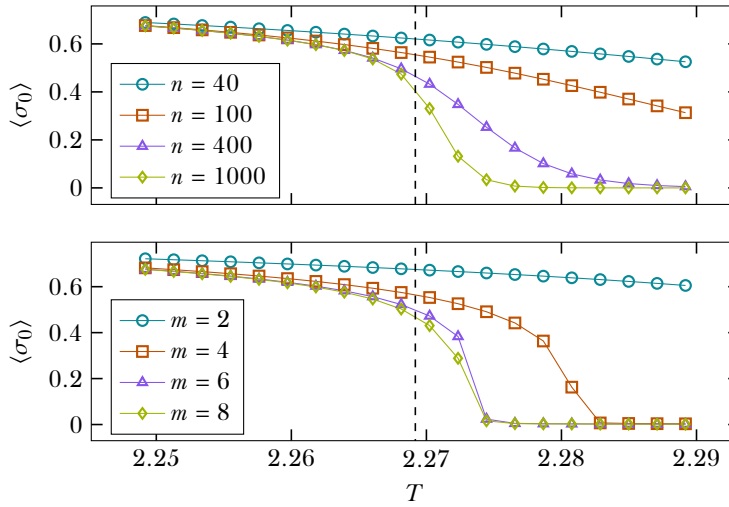

Figure 5.1: Upper panel: expectation value of the central spin $\langle\sigma_0\rangle$ after n CTMRG steps. m is chosen such that the truncation error is smaller than 10^{-6}. Lower panel: $\langle\sigma_0\rangle$ for systems with bond dimension m.

Fig. 5.1 shows the behaviour of the order parameter of the two-dimensional Ising model for systems of finite-size, where the result is converged in m, and for systems of finite m, where the result is converged in the system size N. The results look very similar and support the claim that there are two relevant length scales in the critical region, namely the system size N and the length scale associated to the finite bond dimension m.

5.2 Definition of the effective length scale in terms of the correlation length at T_c

The first direct comparison of finite-size scaling in the system size N with scaling in the bond dimension of the CTMRG method m was done in [7], which proceeds as follows.

In the thermodynamic limit (corresponding to infinite m and N), we have the following expression for the correlation length of a classical system [57]

$$\xi(T) = \frac{1}{\log\left(\frac{T_0}{T_1}\right)}. \tag{5.1}$$

Here, T_0 and T_1 are the largest and second-largest eigenvalues of the row-to-row transfer matrix T, respectively. With N tending towards infinity and finite m, near the critical point $\xi(T)$ should obey a scaling law of the form

$$\xi(T, m) = N_{\text{eff}}(m)\mathcal{F}(N_{\text{eff}}(m)/\xi(T)) \tag{5.2}$$

with

$$\mathcal{F}(x) = \begin{cases} \text{const} & \text{if } x \to 0, \\ x^{-1} & \text{if } x \to \infty. \end{cases} \tag{5.3}$$

Hence, the effective length scale corresponding to the finite bond dimension m is proportional to the correlation length of the system at the critical point $t = 0$.

$$N_{\text{eff}}(m) \propto \xi(T = T_c, m). \tag{5.4}$$

In general, when the location of the critical point is not exactly known, we can make use of Eq. 4.22 to obtain

$$N_{\text{eff}}(m) \propto \xi(T = T^\star(m), m), \tag{5.5}$$

which suffers less from finite-size effects, but is sensitive to the precision of $T^\star(m)$ in the case of a divergent quantity such as the correlation length.

5.3 Relation to finite-entropy scaling and the exponent κ.

The first numerical evidence of a law for the correlation length at the critical point of the form

$$\xi(m) \propto m^\kappa \tag{5.6}$$

was given by the authors of [55], who found

$$\kappa \approx 1.3 \tag{5.7}$$

for a gapless system of free fermions, using DMRG calculations. Later, using the iTEBD algorithm [27], the authors of [29] presented numerical evidence

for such a relation for the Ising model with transverse field and the Heisenberg model, with

$$\kappa_{\text{Ising}} \approx 2, \tag{5.8}$$

$$\kappa_{\text{Heisenberg}} \approx 1.37. \tag{5.9}$$

5.3.1 Quantitative theory for κ

A quantitative theory of the existence of an exponent κ was given in [30]. We reproduce the argument, which is presented in the language of one-dimensional quantum systems, below.

We start by noting that in the critical region, the entanglement of a half-infinite subsystem A diverges as

$$S_A \propto \mathcal{A}(c/6)\log(\xi), \tag{5.10}$$

where $\mathcal{A}$ is the number of boundary points of A and c is the central charge of the conformal field theory at the critical point [23, 58, 59].

Recalling the definition of the entanglement entropy

$$S_A = -\operatorname{Tr}(\rho_A \log \rho_A) = -\sum_\alpha \omega_\alpha \log \omega_\alpha, \tag{5.11}$$

it is trivially seen that the entropy of a state given by the DMRG (or any other MPS), which only retains m basis states of ρ_A, is limited by

$$S_A^{\max}(m) = \log m \tag{5.12}$$

by putting $\omega_\alpha = 1/m$ for $\alpha = 1, \ldots, m$.

This is, incidentally, another way to see that DMRG or CTMRG, or any other algorithm which produces ground states with a matrix-product structure have an inherently finite correlation length.

The leading energy correction to the free energy per site of a one-dimensional quantum system at a conformally invariant critical point at finite temperature T in the thermodynamic limit is [60]

$$f(T) = f_0 + aT^2 + \mathcal{O}(T^3). \tag{5.13}$$

Due to the quantum-classical correspondence, this is equivalent to a two-dimensional classical $N \times \infty$ lattice with strip width $N = 1/T$. This implies

also that the correlation length of a critical one-dimensional quantum system at finite temperature cannot diverge and goes as $\xi \propto 1/T$. In terms of this finite correlation length, Eq. 5.13 is written as

$$f(\xi) = f_\infty + \frac{A}{\xi^2} + \mathcal{O}(\frac{1}{\xi^3}). \tag{5.14}$$

Empirically, optimized ground states with a matrix-product structure at criticality do not simply maximize their entropy, as they should if we take Eq. 5.14 to be true for ground states with a matrix-product structure.

We will now show that Eq. 5.14 needs, in fact, an additional term due to the matrix-product structure with finite bond dimension m.

The ground state with finite correlation length and energy density as in Eq. 5.14 has a Schmidt decomposition that in principle can have infinitely many terms

$$|\psi_0\rangle = \sum_{n=1}^{\infty} \lambda_n |\psi_n^L\rangle |\psi_n^R\rangle, \tag{5.15}$$

where $|\psi_n^L\rangle$ and $|\psi_n^R\rangle$ are states of the left and right infinite half-chains. Normalization requires

$$\sum_{n}^{\infty} \lambda_n^2 = 1. \tag{5.16}$$

The ground state with a matrix-product structure with finite bond dimension m has an additional constraint: its Schmidt decomposition carries only the m $|\psi_n\rangle$ with largest λ_n. It is written as

$$|\psi_0^{\mathrm{MPS}}\rangle = \frac{\sum_{n=1}^{m} \lambda_n |\psi_n^L\rangle |\psi_n^R\rangle}{\sqrt{\sum_{n=1}^{m} \lambda_n^2}}. \tag{5.17}$$

To find the extra energy cost of only keeping the first m terms in the Schmidt decomposition, note that in the limit of m large, $|\psi_0^{\mathrm{MPS}}\rangle$ almost entirely overlaps with $|\psi_0\rangle$, hence can be written as

$$|\psi_0^{\mathrm{MPS}}\rangle = \sqrt{1-\epsilon^2}\,|\psi_0\rangle + \epsilon\,|\psi_{\mathrm{ex}}\rangle, \tag{5.18}$$

where $|\psi_{\mathrm{ex}}\rangle$ is some excited state and $\epsilon \ll 1$. This leads to an energy of

$$E_0^{\mathrm{MPS}} = \langle\psi_0^{\mathrm{MPS}}|\hat{H}|\psi_0^{\mathrm{MPS}}\rangle = E_0 + \epsilon^2(E_{\mathrm{ex}} - E_0), \tag{5.19}$$

with

$$\epsilon^2 = \left(1 - \langle\psi_0|\psi_0^{\mathrm{MPS}}\rangle^2\right) = 1 - \sum_{n=1}^{m} \lambda_n^2 \equiv P_{\mathrm{res}}(m). \tag{5.20}$$

Here, we have defined the residual probability P_{res}, also known as the truncation error, as the part of the spectrum that is thrown away.

If we now assume that $E_0 - E_{\mathrm{ex}}$ is proportional to the energy gap Δ, which scales as [61–63]

$$\Delta \propto \frac{1}{\xi}, \tag{5.21}$$

we arrive at

$$E_0^{\mathrm{MPS}} = E_\infty + \frac{A}{\xi^2} + \frac{BP_{\mathrm{res}}(m)}{\xi}. \tag{5.22}$$

It is clear that when the correlation length is very large, by Eq. 5.10 the entropy and $P_{\mathrm{res}}(m)$ must be too. So, the third term in Eq. 5.22 dominates.

If the correlation length is small, the second term dominates. The correlation length that belongs to the MPS ground state with fixed m is the optimum that minimizes this expression.

The details of the calculation, which can be found in the supplementary material of [30], depend on the asymptotic form of P_{res}, found in [64]. In the limit $m \to \infty$, the correlation is indeed of the form in Eq. 5.6 with

$$\kappa = \frac{6}{c\left(\sqrt{12/c} + 1\right)}, \tag{5.23}$$

which is in good agreement with the values found in [29].

5.4 Locating the critical point with the entanglement spectrum

Since phase transitions of quantum systems can be located by studying their entanglement spectrum [43, 65], classical systems may be investigated in the same way through the correspondence in Eq. 3.57. This is an alternative to the usual approach of studying an order parameter or derivatives of thermodynamical observables.

Examples of studies using the spectrum of the corner transfer matrix to analyze two-dimensional classical systems are [66–68].

At the critical point, the entropy must diverge (cf. Eq. 5.10). For finite systems the entropy will remain finite, but the pseudocritical temperature $T^\star$ is defined as the point of maximum entropy. The critical point is then located by fitting the scaling law in Eq. 4.6.

6
Technical details and convergence behaviour

We describe some technical details of the CTMRG algorithm.

We then report convergence behaviour in the number of steps of the algorithm n and a convergence threshold ϵ. ϵ is based on the change of eigenvalues of the corner transfer matrix after an algorithm step. We find a precise way to extrapolate values of observables in the limit $\epsilon \to 0$.

After that, we turn to finite-size approximations. Convergence in the limit $m \to \infty$ is harder to extrapolate, but we can still draw some conclusions.

Finally, we give a table with relative errors of observables at the critical point of the Ising model for both finite-m and finite-size approximations, obtained with values of parameters that are typically used throughout the rest of this thesis.

6.1 Symmetricity and normalization of tensors

For the models treated in this thesis, the corner transfer matrix A and the row-to-row transfer matrix T are symmetric. But due to the accumulation of machine-precision sized errors in the matrix multiplication and singular value decomposition, this will, after many algorithm steps, no longer be the case. In order for results to remain valid, we manually enforce symmetricity after each step.

The tensor network contractions at each algorithm step will cause the elements of A and T to tend to infinity, which means that they will at some point exceed the maximum value of a floating point number as it can be stored in memory. But because the elements of A and T represent Boltzmann weights, they can be scaled by a constant factor, which allows us to prevent this overflow if we use a suitable scaling. For example by requiring that

$$\mathrm{Tr}\, A^4 = 1, \tag{6.1}$$

so that the interpretation of A^4 as a reduced density matrix of an effective one-dimensional quantum is valid.

6.2 Boundary conditions

Unless otherwise stated, all simulations are run with the boundary spins of the lattice fixed to +1. For specific purposes, free boundary conditions are used.

6.3 Convergence criteria

6.3.1 Simulations with finite bond dimension

The convergence of the CTMRG algorithm with fixed bond dimension m (the infinite system algorithm) in this thesis is defined as

$$c_n = \sum_{\alpha=1}^{m} |s_\alpha^{(n)} - s_\alpha^{(n-1)}|, \tag{6.2}$$

where s_α are the singular values of the corner transfer matrix A. If the convergence falls below some threshold ϵ, the algorithm terminates.

The assumption is that once the singular values stop changing to some precision, the optimal projection is sufficiently close to its fixed point and the transfer matrices A and T represent an environment only limited by the length scale given by m, i.e.

$$\xi(m) \ll N \tag{6.3}$$

is satisfied.

6.3.1.1 Convergence at the critical point of the Ising model

The convergence is shown in Fig. 6.1. It is clear that the phenomenological law

$$\log c_n \propto n \tag{6.4}$$

holds to high precision, with the slope depending on m. Deviations only occur at values of the convergence of around 10^{-12}.

The convergence of the various quantities as function of the number of algorithm steps is shown in Fig. 6.2. For all quantities Q, the absolute value

of the relative difference with the final algorithm step

$$\Delta Q_{\text{rel}}(n) = \left| \frac{Q(n) - Q(n = 10^5)}{Q(n = 10^5)} \right| \tag{6.5}$$

is shown. Again, a law of the form

$$\log(\Delta Q_{\text{rel}}) \propto n \tag{6.6}$$

seems to hold.

To make an estimate of a quantity in the limit $N \to \infty$, or equivalently $\epsilon \to 0$, we can study the change in a quantity as function of the convergence threshold ϵ. We define

$$\Delta Q_{\text{step}}(\epsilon) = Q(\epsilon) - Q(10\epsilon), \tag{6.7}$$

i.e. the change of quantity Q when we decrease the threshold ϵ by an order of magnitude. The results in Fig. 6.3 show that, the order parameter, entropy and correlation length to high precision follow the linear relationship

$$\Delta Q_{\text{step}}(\epsilon) = \alpha_Q(m)\epsilon, \tag{6.8}$$

whereas the free energy follows a quadratic relationship

$$\Delta f(\epsilon) = \alpha_f(m)\epsilon^2. \tag{6.9}$$

This means that we can confidently extrapolate the value of a quantity in the fully converged limit as

$$Q(\epsilon \to 0) = Q(\epsilon_{\min}) + \sum_{\epsilon = \frac{\epsilon_{\min}}{10}, \frac{\epsilon_{\min}}{100}, \ldots} \Delta Q_{\text{step}}(\epsilon), \tag{6.10}$$

where $\epsilon_{\min}$ is the lowest threshold used in simulation, and $\Delta Q_{\text{step}}(\epsilon)$ is determined by fitting to suitable higher values of the threshold.

6.3.2 Simulations with finite system size

In the finite-system algorithm, we want to reliably extrapolate quantities in the bond dimension m. The convergence behaviour is shown in Fig. 6.4. For

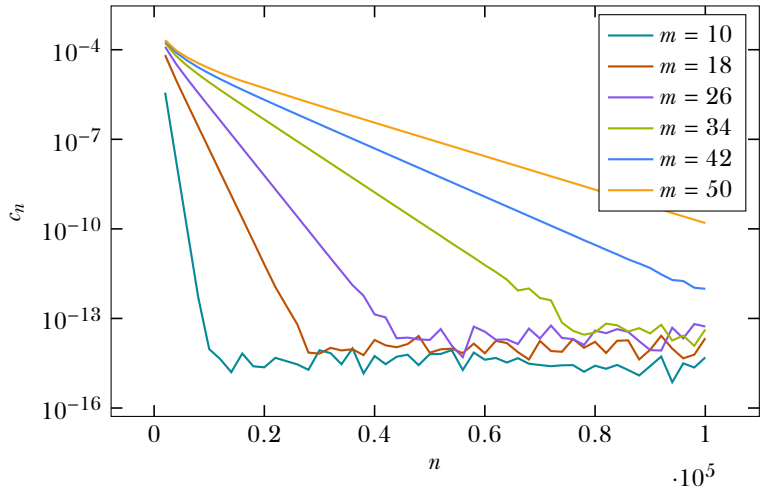

Figure 6.1: Convergence as defined in Eq. 6.2 versus n, the number of CTMRG steps. Up until very small values of c_n, the convergence is monotonically decreasing and obeys a logarithmic law with slope depending on m.

each quantity Q, we plot the absolute value of the relative difference with the value at the highest m

$$\Delta Q_{\text{rel}}(m) = \left| \frac{Q(m) - Q(m = 200)}{Q(m = 200)} \right| \tag{6.11}$$

versus the bond dimension m.

The plateaus of m-values that barely increase the precision are due to the structure in the spectrum of the reduced density matrix. Apart from this noise, the law

$$\Delta Q_{\text{rel}}(m) \propto m^{\alpha(N)} \tag{6.12}$$

is seen to hold for high enough m for the order parameter, free energy and entropy.

To extrapolate to $m \to \infty$, analogously to the finite-m case we define

$$\Delta Q_{\text{step}}(m) = Q(m) - Q(m-1), \tag{6.13}$$

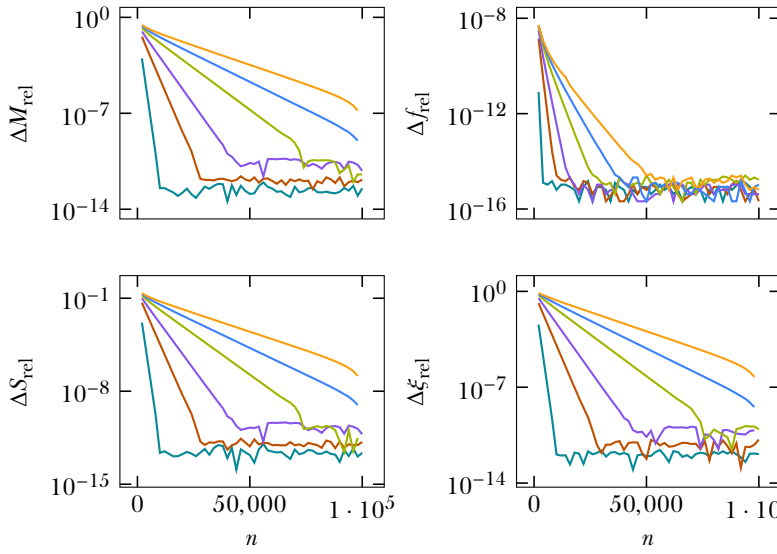

Figure 6.2: Absolute value of relative difference of quantities (see Eq. 6.5). Same legend as Fig. 6.1.

which is plotted in the left panel of Fig. 6.5. As expected from Eq. 6.12, the overall trend looks like a power law, but the noise makes it hard to determine it accurately. It is anyway neither practical nor needed to calculate a system of finite size for many consecutive values of m, in order to get a good approximation to Eq. 6.13. Instead, one might compute the quantity for equally spaced values of m with a difference of say, 10 or 20.

As described in section 3.7 and in [45, 47, 48], for the off-critical Ising model the degeneracies in the corner transfer matrix A are exactly known. These degeneracies are smoothed out, but not completely lost for finite systems near criticality. This is directly related to the convergence of quantities in m.

As an alternative to Eq. 6.13, it might be conjectured that not a fixed increase of m, but taking all basis states corresponding to the next energy level will increase accuracy in a predictable way.

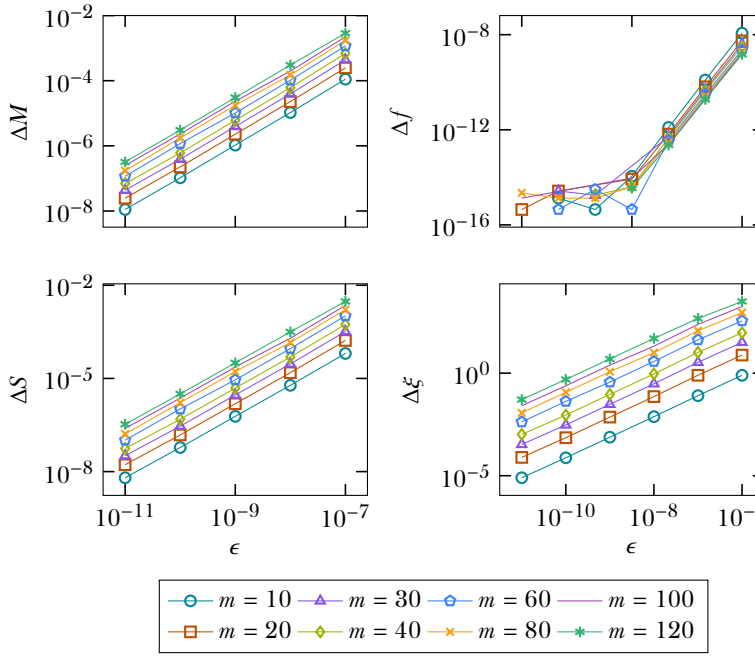

Figure 6.3: Stepwise differences upon decreasing the threshold ϵ by an order of magnitude, as in Eq. 6.7. For the order parameter, entropy and correlation length, a linear relationship holds to high precision, while for the free energy the relationship is quadratic.

This suspicion is confirmed in the right panel of Fig. 6.5, which shows the convergence using only the values of m for which all basis states with a certain energy level are present, i.e. [48]

$$m(j) = \sum_{k=0}^{k=j} p(k). \tag{6.14}$$

The first few values of $m(j)$ are

$$1, 2, 3, 5, 7, 10, 14, 19, 25, 33, 43, 55, 70, 88, 110, 137, 169, 207, \ldots \tag{6.15}$$

Using these values of m, the result is again a power law, and the noise largely disappears, but the convergence behaviour is still not devoid of structure entirely.

The error on a quantity calculated at bond dimension $m_{\max}$ can be approximated as

$$M(m \to \infty) = M(m_{\max}) + \sum_{\text{higher values of } m} \Delta Q_{\text{step}}(m), \tag{6.16}$$

where ΔQ_{step} is fitted from aptly chosen lower values of m.

6.4 Values of hyperparameters for the Ising model

We have found that for practical purposes, in the infinite-system algorithm the convergence threshold ϵ may be set to 10^{-7} for values of m below, say, 30, and to 10^{-8} for m-values above 40. For the highest value of $m = 120$, this leads to a relative error, as compared with the theoretically fully converged limit $\epsilon \to 0$, of about 0.1% in the correlation length, and less than 0.02% in the order parameter, entropy and free energy (the relative error on the free energy being basically zero). For lower values of m, the relative errors are substantially lower. See Table 6.1.

For simulations of finite systems, we have found that choosing m such that the truncation error P_r (for *residual probability*, its other common name) is smaller than 10^{-6} is sufficient for most purposes. This leads to a relative error with the fully converged limit $m \to \infty$ of at most 0.06% in the order parameter, entropy and free energy for $n = 8000$. For lower values of N, the relative error is lower. Here, we have taken the order parameter as the main benchmark, since the correlation length is not used for finite-size calculations. See Table 6.2.

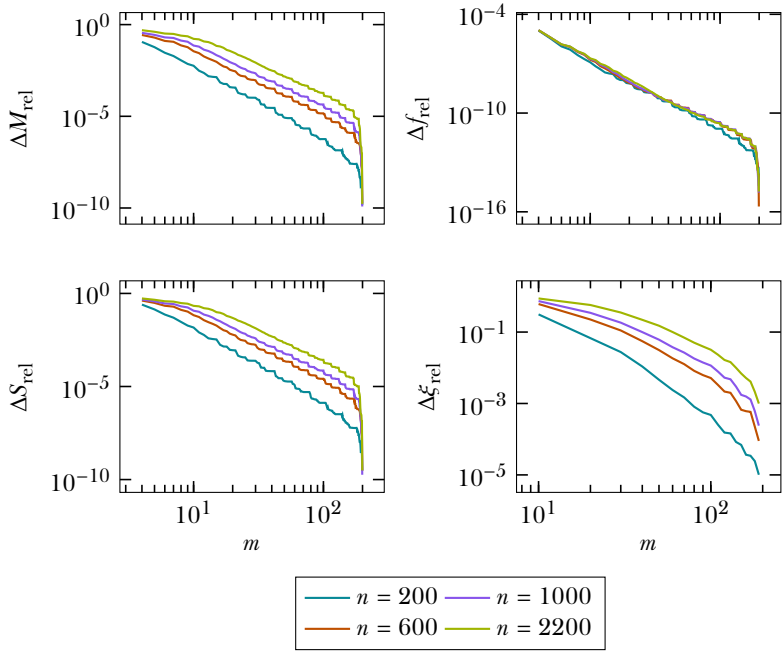

Figure 6.4: The absolute value of the relative difference of quantities, as defined in Eq. 6.11. For high enough m, it obeys a power law with varying exponent $\alpha(N)$. The sharp drop for the highest values of m is an artefact of the definition of ΔQ_{rel} and the plateau-like fashion in which the value of a quantity converges, owing to the spectrum of the reduced density matrix approximated by the CTMRG algorithm. Like in the finite-m case, the free energy converges much faster than the other quantities, and does so with little n-dependence. Note that $\Delta \xi_{\mathrm{rel}}$ does not obey a power law.

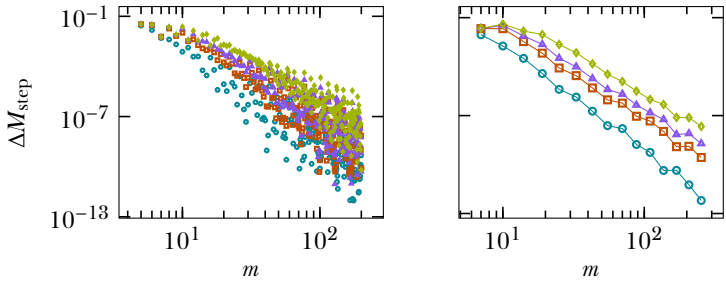

Figure 6.5: Same legend as Fig. 6.4

m	rel. error % ($\epsilon = 10^{-7}$)	rel. error % ($\epsilon = 10^{-8}$)
40	0.02	0.02
80	0.6	0.05
120	1.1	0.1

Table 6.1: Relative errors of $\xi(T_c, m, \epsilon)$, as compared with the fully converged limit $\epsilon \to 0$, approximated by Eq. 6.10.

n	rel. error % ($P_r < 10^{-5}$)	rel. error % ($P_r < 10^{-6}$)	rel. error % ($P_r < 10^{-7}$)
1000	0.08 (40)	0.005 (80)	0.001 (120)
2000	0.08 (60)	0.008 (100)	0.002 (160)
8000	0.6 (80)	0.07 (140)	0.005 (280)

Table 6.2: Relative errors of $M(T_c, n)$, calculated such that the truncation error P_r does not exceed listed threshold, as compared with the fully converged limit of $m \to \infty$ (zero truncation error), approximated by Eq. 6.16. The number in brackets is the value of m used. To approximate the error, steps in m-value of 5, 10 or 20 were used, depending on $m_{\max}$.

7
Numerical results for the Ising model

We present numerical results of finite-m and finite-size scaling within the CTMRG method on the Ising model.

With finite-m simulations, it is much easier to reach large system sizes, but thermodynamic quantities do not grow smoothly as a function of m, as a result of the underlying spectrum of the corner transfer matrix. This makes it harder to fit the basic power law divergences. Defining the correlation length in terms of the classical analogue to the entanglement entropy mitigates this effect somewhat.

Quantities calculated with finite-size simulations do not suffer this unsmooth behaviour. Results for both methods are comparable, but it is plausible that finite-size data turns out to be more accurate when corrections to scaling are included.

Apart from thermodynamic quantities, we also accurately compute the central charge of the critical point with both methods. Additionally, we verify the relation $\xi(m) \propto m^{\kappa}$ at the critical point, although the value of κ found in this work is slightly lower than predicted in the literature.

7.1 At the critical point

7.1.1 Existence of two length scales

First, we reproduce the results presented in [7] to validate the assumption that at the critical point, the only relevant length scales are the system size N and the length scale associated to a finite dimension m of the corner transfer matrix $\xi(m)$. Here, we assume that $\xi(m)$ is given by the correlation length at the critical point, see section 5.2.

The order parameter[1] should obey the following scaling relation at the

[1] It is worth stressing that the order parameter and the magnetization per site are used inter-

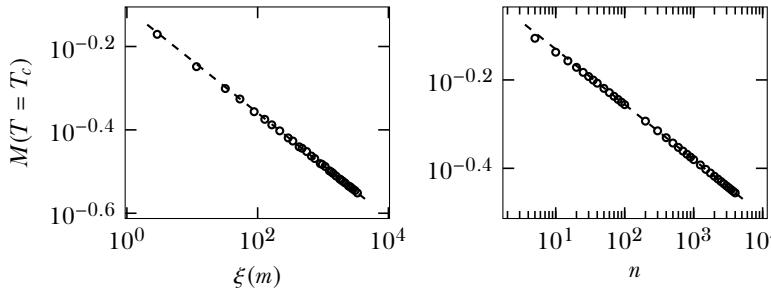

Figure 7.1: Left panel: fit to the relation in Eq. 7.1, yielding $\frac{\beta}{\nu} \approx 0.125(5)$. The data points are obtained from simulations with $m = 2, 4, \ldots, 64$. The smallest 10 values of m have not been used for fitting, to diminish correction terms to the basic scaling law. Right panel: fit to conventional finite-size scaling law given in Eq. 7.2, fitted with $n = 1500, 1750, \ldots, 4000$, calculated with a truncation error no larger than 10^{-7}, yielding $\beta/\nu \approx 0.1249$.

critical temperature

$$M(T = T_c, m) \propto \xi(T = T_c, m)^{-\beta/\nu}. \tag{7.1}$$

The left panel of Fig. 7.1 shows that this scaling relation holds. The fit yields $\frac{\beta}{\nu} \approx 0.125(5)$, close to the true value of $\frac{1}{8}$.

The right panel shows the conventional finite-size scaling relation

$$M(T = T_c, N) \propto N^{-\beta/\nu}, \tag{7.2}$$

yielding $\beta/\nu \approx 0.1249(1)$.

The correlation length $\xi(m)$ shows characteristic half-moon patterns on a log-log scale, stemming from the smeared-out stepwise pattern in the corner transfer matrix spectrum (see section 3.7). This makes the data harder to interpret, since the effect of increasing m depends on how much of the spectrum is currently retained.

changeably for the Ising model, and that the magnetization per site is approximated, within the CTMRG algorithm, by the expectation value of the central spin. See section 3.6.2.

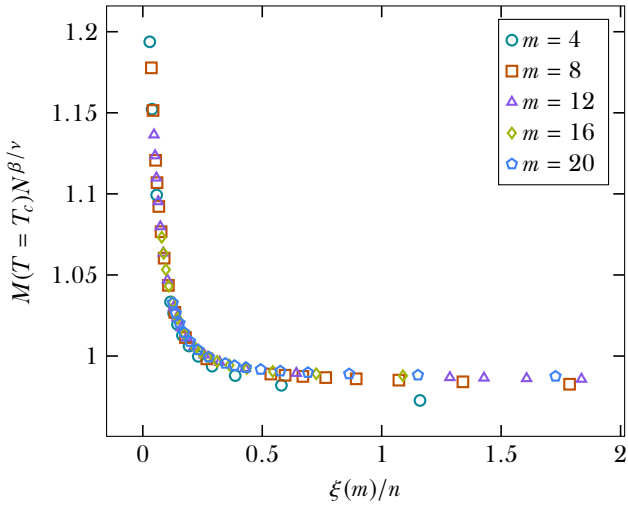

Figure 7.2: Scaling function $\mathcal{G}(\xi(m)/N)$ given in Eq. 7.3.

To further test the hypothesis that N and $\xi(m)$ are the only relevant length scales, the authors of [7] propose a scaling relation for the order parameter M at the critical temperature of the form

$$M(N, m) = N^{-\beta/\nu}\mathcal{G}(\xi(m)/N) \tag{7.3}$$

with

$$\mathcal{G}(x) = \begin{cases} \text{const} & \text{if } x \to \infty, \\ x^{-\beta/\nu} & \text{if } x \to 0, \end{cases} \tag{7.4}$$

meaning that Eq. 7.3 reduces to Eq. 7.2 in the limit $\xi(m) \gg N$ and to Eq. 7.1 in the limit $N \gg \xi(m)$. Fig. 7.2 shows that the scaling relation of Eq. 7.3 is justified.

Fig. 7.3 shows the cross-over behaviour from the N-limiting regime, where $M(N, m) \propto N^{-\beta/\nu}$ to the $\xi(m)$-limiting regime, where $M(N, m)$ does not depend on N.

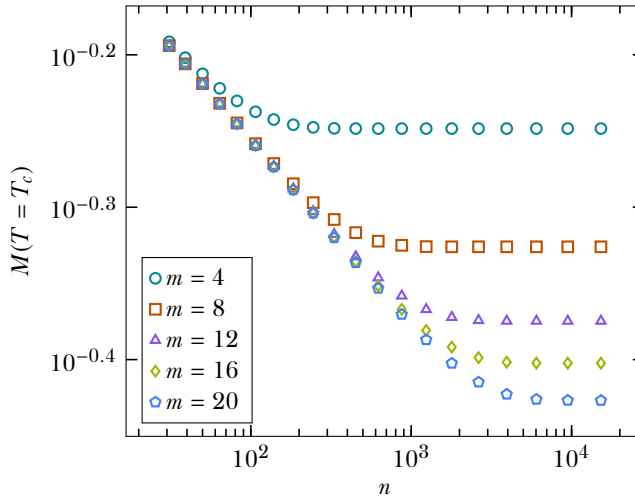

Figure 7.3: Behaviour of the order parameter at fixed m as function of the number of renormalization steps n. For small n, all curves coincide, since the system size is the only limiting length scale. For large enough n, the order parameter is only limited by the length scale $\xi(m)$. In between, there is a cross-over described by $\mathcal{G}(\xi(m)/N)$, given in Eq. 7.3.

7.1.2 Central charge

We may directly verify the value of the central charge c associated with the conformal field theory at the critical point by fitting to

$$S_{\text{classical}} \propto \frac{c}{6} \log \xi(m), \tag{7.5}$$

which yields $c = 0.501$, shown in the left panel of Fig. 7.4.

The right panel of Fig. 7.4 shows the fit to the scaling relation in N (or, equivalently the number of CTMRG steps n)

$$S_{\text{classical}} \propto \frac{c}{6} \log N, \tag{7.6}$$

which yields $c = 0.499$.

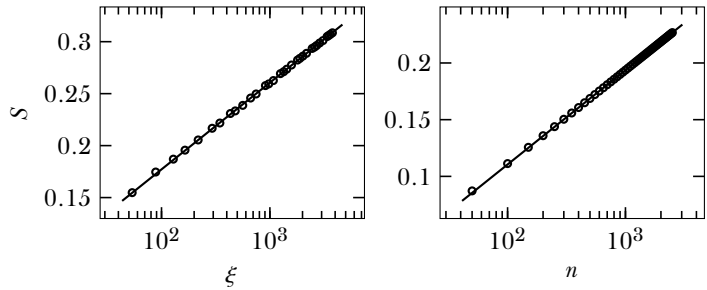

Figure 7.4: Left panel: numerical fit to Eq. 7.5, yielding $c = 0.501$. Here, $m \in \{8, 10, \ldots, 70\}$ and the convergence threshold $\epsilon = 10^{-9}$. Right panel: numerical fit to Eq. 7.6, yielding $c = 0.499$, with the fit made to $n \in \{1500, 1550, \ldots 2500\}$, such that the truncation error is smaller than 10^{-7}.

7.1.3 Using the entropy to define the correlation length

Via Eq. 5.10, the correlation length is expressed as

$$\xi \propto \exp(\frac{6}{c}S). \tag{7.7}$$

Fig. 7.5 shows the results of fitting the relation in Eq. 7.1 with this definition of the correlation length. The fit is an order of magnitude better in the least-squares sense, and the half-moon shapes have almost disappeared, yielding a much more robust exponent of $\beta/\nu = 0.12498$.

The entropy uses all eigenvalues of the corner transfer matrix, making it apparently less prone to structure in the spectrum than the correlation length as defined in Eq. 5.1, which uses only two eigenvalues of the row-to-row transfer matrix. Furthermore, the corner transfer matrix A is kept diagonal in the CTMRG algorithm, so S is much cheaper to compute than ξ.

7.1.4 Exponent κ

We now check the validity of the relation

$$\xi(m) \propto m^{\kappa} \tag{7.8}$$

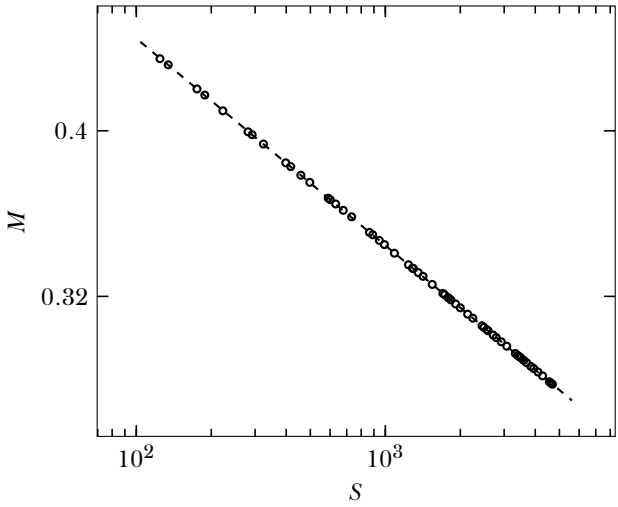

Figure 7.5: Fit to Eq. 7.1, using Eq. 7.7 as the definition of the correlation length. For the fit, we have used $m \in \{10, 11, \ldots, 66\}$, calculated with convergence threshold $\epsilon = 10^{-9}$, yielding $\beta/\nu = 0.12498$.

in the context of the CTMRG method for two-dimensional classical systems. Similar checks were done for one-dimensional quantum systems in [29].

Let us first state that boundary conditions are relevant. From section 3.7 we expect that for fixed boundary conditions, the entropy and therefore the correlation length is lower for a given bond dimension m.

There are various ways of extracting the exponent κ. Fig. 7.6 shows the results for fixed boundary conditions and Fig. 7.7 for free boundary conditions.

Directly checking Eq. 7.8 yields $\kappa = 1.93$ for a fixed boundary and $\kappa = 1.96$ for a free boundary.

Under the assumption of Eq. 7.8, we have the following scaling laws at the

critical point

$$M(m) \propto m^{-\beta\kappa/\nu} \tag{7.9}$$

$$f(m) - f_{\text{exact}} \propto m^{(2-\alpha)\kappa/\nu} \tag{7.10}$$

for the order parameter and the singular part of the free energy, respectively. With a fixed boundary, a fit to $M(m)$ yields $\kappa = 1.93$. For a free boundary we cannot extract any exponent, since $M = 0$ for every temperature. A fit to $f(m) - f_{\text{exact}}$ yields $\kappa = 1.90$ for a fixed boundary and $\kappa = 1.93$ for a free boundary. Fig. 7.6. Here, we have used $\beta = 1/8$, $\nu = 1$ and $\alpha = 0$ for the Ising model.

We may use Eq. 5.10 and Eq. 3.58 to check the relation

$$S_{\text{classical}} \propto \frac{c\kappa}{6} \log m, \tag{7.11}$$

which yields $\kappa = 1.93$ for a fixed boundary and $\kappa = 1.96$ for a free boundary, with $c = 1/2$ for the Ising model.

7.1.4.1 Comparison with exact result in asymptotic limit

The predicted value for κ [30] is $2.034\ldots$ (see also Eq. 5.23). With the CTMRG method, we extract the slightly lower value of 1.96 (corresponding to free boundary conditions). But, the structure in the quantities as function of m makes it hard to get an accurate fit to κ.

It is interesting to note that for fixed boundary conditions, the relation in Eq. 7.8 holds, but with a lower exponent κ. This is to be expected, since half the spectrum of the corner transfer matrix is missing.

7.2 Locating the critical point

In general, the critical point is not known, but it may be located by extrapolating the position of the pseudocritical temperature at finite system sizes.

The pseudocritical point can be defined in a variety of ways. In this chapter, we will define the pseudocritical point as the point of maximum entropy, as described in section 5.4. Fig. 7.8 shows the classical analogue to the entanglement entropy as a function of temperature for different values of m.

The critical point is located by fitting the scaling law in Eq. 4.6.

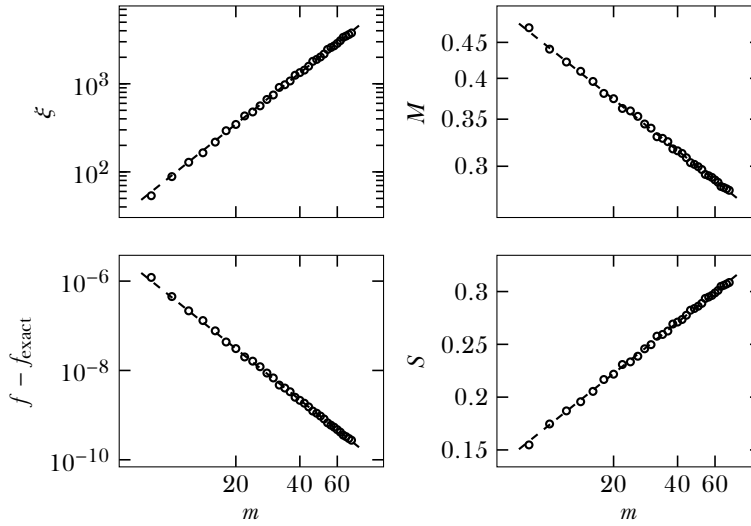

Figure 7.6: Numerical evidence for Eq. 7.8, Eq. 7.9, Eq. 7.11 with fixed boundary, yielding, from left to right and top to bottom, $\kappa = \{1.93, 1.93, 1.90, 1.93\}$. These values have been calculated from simulations with $m \in \{8, 10, \ldots, 70\}$ and convergence threshold $\epsilon = 10^{-9}$.

7.2.1 Finite m

For approximations with finite bond dimension m, we may use different length scales to fit the scaling behaviour of $T^\star(m)$. In light of the discussion in section 5.2, we can choose either $\xi(T_c, m)$ or $\xi(T^\star(m), m)$. The latter suffers less from finite-size effects, but is dependent on the accuracy with which $T^\star$ is located. It is, of course, of more general interest since T_c is normally not known.

Furthermore, we will consider both $\xi(m)$ derived from the row-to-row transfer matrix (Eq. 5.1) and derived from the entanglement entropy (Eq. 7.7).

Fig. 7.9 shows the fits for different choices of this length scale. The results are tabulated in Table 7.1. To obtain $T^\star$, we have calculated $T^\star(m)$ for $m \in \{10, 11, \ldots, 60\}$ with a convergence threshold of 10^{-8} and a temperature tolerance of 10^{-8}. The boundaries are fixed to +1.

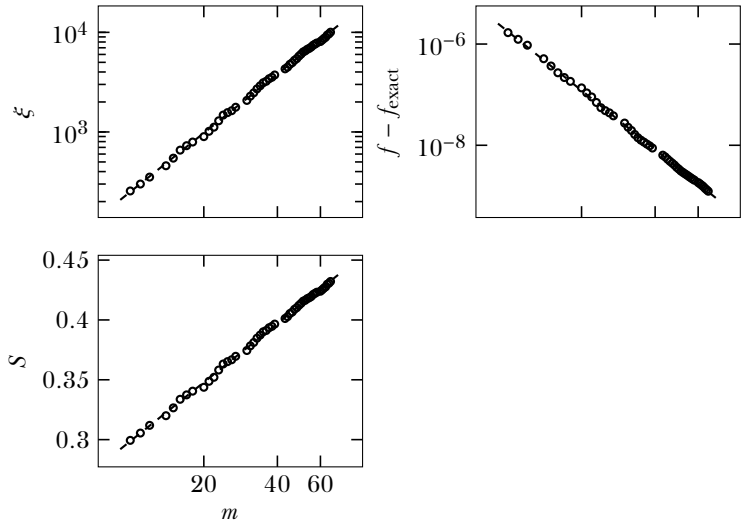

Figure 7.7: Numerical evidence for Eq. 7.8 with free boundary, yielding from left to right and then bottom $\kappa = \{1.96, 1.93, 1.96\}$. These values have been calculated from simulations with $m \in \{10, 11, \ldots, 66\}$, but with $m \in \{13, 19, 28, 29, 40, 41, 42, 59\}$ left out, because for those values m the system breaks its symmetry (see section 3.7.2). The convergence threshold was chosen to be $\epsilon = 10^{-7}$. It is not feasible to choose a lower threshold since more values of m break symmetry as machine precision is approached.

We denote the estimated value of the critical temperature as $\widetilde{T_c}$. Recall that the exact value is

$$T_c = 2.2691853\ldots \tag{7.12}$$

and

$$\nu = 1. \tag{7.13}$$

When using $\xi(T_c, m)$, the correlation length at the exact critical point, the result shows a lot of structure, yielding $\widetilde{T_c} = 2.269172$ and $\nu = 1.057$.

N_{eff}	T_c	ν
$\xi(T_c, m)$	2.269172	1.057
$\xi(T^\star(m))$	2.269183	1.002
$\exp((6/c)S(T^\star(m))$	2.269183	1.02
m^κ	2.269181	–
N	2.269185	0.98

Table 7.1: Results for fits to the scaling law Eq. 4.6 using different length scales. When using m^κ, $\kappa \approx 1.91$ was found to give the best fit.

If, instead, the correlation length at the estimated pseudocritical temperature $\xi(T^\star(m))$ is used, the data shows less structure and we obtain the much more precise results $\widehat{T_c} = 2.269183$ and $\nu = 1.002$.

Another option is to use the entropy to define the correlation length, via Eq. 7.7, which gave more accurate results than using the transfer matrix definition in section 7.1.3. In this case, the results are slightly worse than the transfer matrix definition: $T_c = 2.269183$ and $\nu = 1.02$.

Finally, we may directly fit the law

$$|T_c - T^\star(m)| \propto m^{-\kappa/\nu}, \tag{7.14}$$

yielding $T_c = 2.269181$ and $\kappa/\nu = 1.91$. Incidentally, this is another way to confirm $\kappa \approx 1.9$ for systems with a fixed boundary.

7.2.2 Finite N

As a cross check, we can instead use systems of finite size to extract T_c and ν. We have calculated $T^\star(n)$ for $n \in \{2300, 2500, \ldots, 7900\}$, with m big enough such that the truncation error is no larger than 10^{-6}. This yields $T_c = 2.269185$ and $\nu = 0.98$.

7.3 Away from the critical point

We may also verify the validity of the different length scales by asserting that the data for different values of m should collapse on a single curve

$$\mathcal{G}(t\xi(m)^{1/\nu}) = M(T, m)\xi(m)^{\beta/\nu}. \tag{7.15}$$

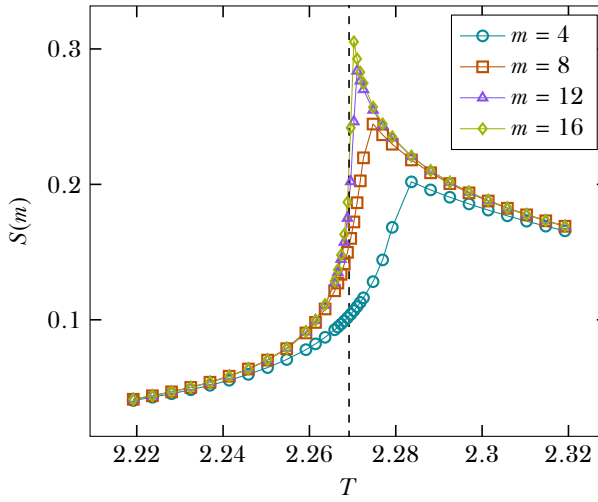

Figure 7.8: Classical analogue to the entanglement entropy, as in Eq. 3.58, near the critical point (shown as dashed line).

All data points were calculated with a convergence threshold of 10^{-7}. The values of the pseudocritical temperatures are taken from the results in section 7.2. No temperatures beyond T_c is considered because the order parameter drops off sharply, causing the curve $\mathcal{G}(x)$ to tend to zero almost vertically, making the fitness P unreliable.

Fig. 7.10 shows that for all length scales, the results more or less fall on one curve. Table 7.2 shows the fitness of the data collapse [54] (given by Eq. 4.27) for all length scales used.

Using m^κ as a length scale for optimized fitness $P(\kappa)$ yields $\kappa \approx 1.98$, substantially higher than found previously for fixed boundary conditions.

As a cross-check, the bottom-right panel of Fig. 7.10 shows data points for finite-N simulations. Here, the bond dimension is chosen such that the truncation error is smaller than 10^{-6}.

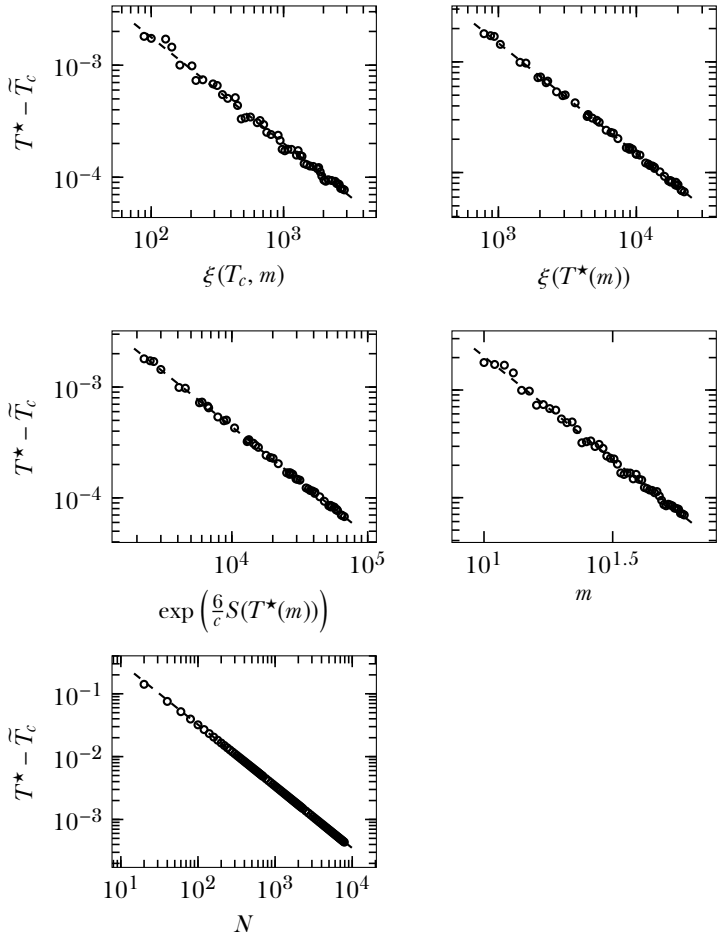

Figure 7.9: Fits to the scaling law Eq. 4.6. Results for the critical temperature and exponent ν are tabulated in Table 7.1.

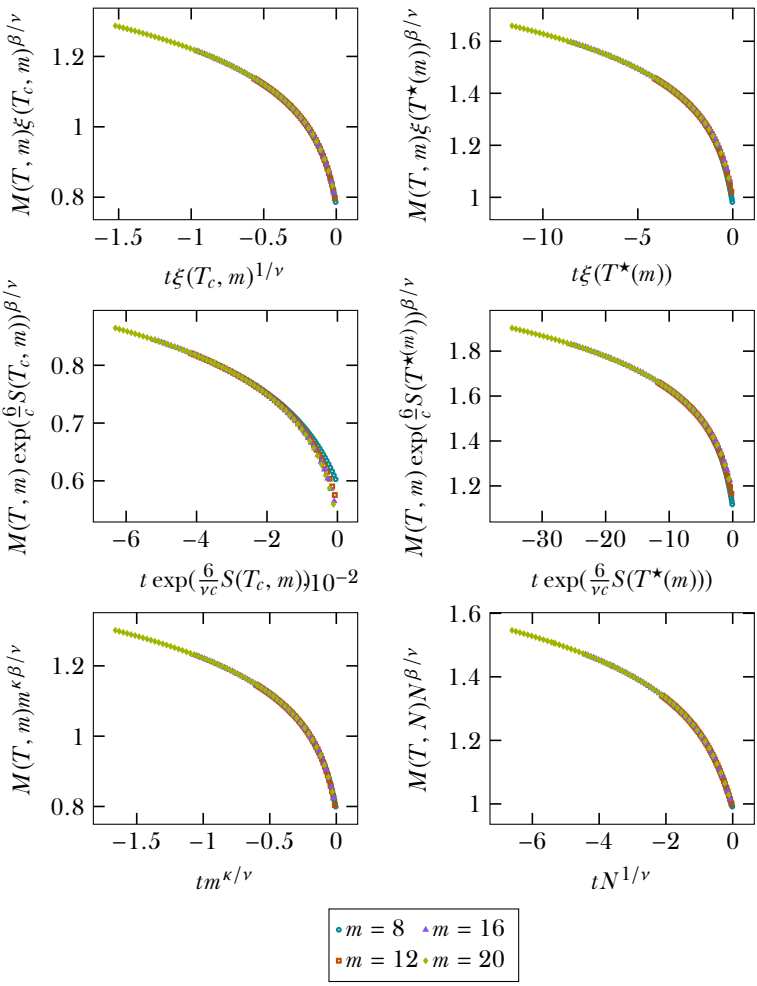

Figure 7.10: Data collapses using different length scales. For the bottom-right plot, approximations with finite N instead of finite m have been used, with $n = \{160, 480, 1000, 1500\}$ ($n = \frac{N-1}{2}$ is the number of algorithm steps).

N_{eff}	fitness P
$\xi(T_c, m)$	0.0075
$\xi(T^\star(m))$	0.066
$\exp((6/c)S(T_c, m))$	0.057
$\exp((6/c)S(T^\star(m))$	0.087
m^κ	0.0080
N	0.0075

Table 7.2: Fitness of data collapse (Eq. 4.27) for different length scales. $\kappa \approx 1.98$ was found to be optimal for the length scale m^κ.

7.4 Discussion

7.4.1 Finite-m vs finite-size simulations

With finite-m simulations, larger system sizes are accessible. This is clearly seen from the fact that for modest values of m, $T^\star(m)$ is already closer to the critical point than $T^\star(N)$ for the largest values of N.

For the Ising model, finite-size and finite-m scaling give comparable results. However, finite-size data is of much higher quality than the finite-m data, since the latter suffers from structure due to the spectrum of the corner transfer matrix, even when defining the correlation via the entanglement entropy. Therefore, it is likely that finite-size results improve significantly if correction to scaling terms are included in the fits.

For finite-size simulations, it is not entirely clear how the chosen bond dimension (and correspondingly, the truncation error) influences the precision of quantities and the position of the pseudocritical point. This could be analysed more thoroughly. A start with this has been made in section 6.3.2.

It might be possible to simulate larger system sizes without much loss of accuracy, but it seems unlikely that the same system sizes as in the finite-m regime are accessible.

For finite-m results it is much easier to assess the convergence of quantities (see section 6.3.1). The quality of the fit remains limited by the structure that is inherent in the data.

7.4.2 Exponent κ

We consistently find a value for the exponent κ that is between 1.93 and 1.96 (for simulations with free boundary conditions), while the theoretically predicted value is approximately 2.034.

The first reason for this might simply be the fact that the data has half-moon shaped patterns that make it hard to extract an exponent reliably.

A second possibility is that, since the predicted value for κ is only valid in the limit $m \to \infty$, finite-m effects cause the exponent obtained from numerical simulation to be lower. This is confirmed by the authors of [30], who use the iTEBD algorithm [27] to obtain $\kappa = 1.92$ for the Ising model and $\kappa = 1.26$ for the XXZ model (predicted value $1.34\ldots$), among other results. However, the authors of [29] consistently find $\kappa \approx 2$ for the Ising model using iTEBD.

A third possibility is that the corner transfer matrices used for the calculations in this work do not represent optimal matrix-product states. In theory, the CTMRG algorithm should produce an optimized row-to-row transfer matrix with matrix product structure in the thermodynamic limit [2]. But because simulations with free boundary conditions are sensitive to numerical errors, we could only choose a moderately low convergence threshold. This might in part explain the observed discrepancy.

8
Numerical results for the clock model

We present a numerical study of the square-lattice clock model with $q = \{5, 6\}$ states. We employ the corner transfer matrix renormalization group method, working in both finite-size and finite-m regimes.

The model has a low-temperature ordered phase, a massless phase and a high-temperature disordered phase. We locate the transition temperatures T_1 and T_2 by extrapolating the positions of pseudocritical temperatures, assuming the transitions are of the Kosterlitz-Thouless type.

The pseudocritical temperature is defined as the point where the classical analogue of the entanglement entropy reaches its maxixum. For free (fixed) boundary conditions the entropy peaks near T_1 (T_2).

In addition, we calculate the central charge and the magnetization exponent in the massless phase. In comparison with exact results for the Villain formulation, the magnetization exponent suggests that the locations of T_1 and T_2 found in this work might underestimate the extent of the massless phase, but we argue it is plausible that this is due to finite-size effects.

8.1 Introduction

In the field of phase transitions and critical phenomena, the two-dimensional topological phase transition discovered by Kosterlitz and Thouless [69, 70] receives much attention. This phase transition is characterized not by an order parameter which indicates a breaking of symmetry, but by the proliferation of topological defects.

In the low-temperature phase, the two-point correlation functions decay with a power-law with varying exponent $\eta(T)$. At the transition, the correlation length diverges as

$$\xi \propto \exp(A|T - T_c|^{-1/2}), \tag{8.1}$$

with A a non-universal constant. Above the transition, the two-point correlators decay exponentially.

The XY model consists of planar rotors on the square lattice. It exhibits the Kosterlitz-Thouless (KT) phase transition and by the Mermin-Wagner-Hohenberg theorem the symmetry of the ground state is broken for all temperatures, due to the $O(2)$ (planar rotational) symmetry of the potential [71, 72].

The q-state clock model possesses the discrete $\mathbb{Z}_q$ symmetry and is an interpolation between the Ising model, which corresponds to $q = 2$, and the XY model, which corresponds to $q \to \infty$. Its energy function is given by

$$H_q = -\sum_{\langle ij \rangle} \cos(\theta_i - \theta_j), \tag{8.2}$$

with the spins taking the values

$$\theta = \frac{2\pi n}{q} \qquad n \in \{0, \ldots, q-1\}. \tag{8.3}$$

It has been proven that for high enough q, this model indeed exhibits a Kosterlitz-Thouless transition [73]. Furthermore, it has been proven that for $q \geq 5$, a general model with $\mathbb{Z}_q$ symmetry (of which Eq. 8.2 is a special case) has three phases: a symmetry broken phase for $T < T_1$, an intermediate phase with power law decay of the correlation function, and a high-temperature phase with exponential decay of the correlation function for $T > T_2$ [74].

In the Villain formulation of the potential [75], it has been proven that the transition at T_2 is a BK-transition [76], and numerical results suggest that for a broad range of temperatures, the thermodynamic behaviour becomes identical to the XY model for high enough q [77].

Furthermore, in the Villain formulation it is known that [78, 79]

$$\eta(T_1) = \frac{4}{q^2}, \qquad \eta(T_2) = \frac{1}{4}, \tag{8.4}$$

where η is the spin-spin correlation function exponent. In CTMRG simulations, it is possible to obtain this exponent through the relation

$$\frac{\eta}{2} = \frac{\beta}{\nu}, \tag{8.5}$$

where the fraction $\frac{\beta}{\nu}$ is found by finite-size scaling of the magnetization (see section 4.2.1).

For the cosine model in Eq. 8.2, the value q_c for which it first exhibits a BK-transition is not precisely known. There is some disagreement about whether the cases $q = 5, 6$ exhibit KT-type transitions (see previous numerical results below).

In our simulations we will focus on the cases $q = 5, 6$, to (i) study the nature of the phase transition from the new perspective provided by the corner transfer matrix formalism and (ii) compare the accuracy of finite-m and finite-N scaling within the CTMRG method to other established numerical methods.

We summarise previous numerical results, then present results obtained with the CTMRG algorithm and finish with a discussion.

8.2 Previous numerical results

8.2.1 The $q = 5$ clock model

The general consensus is that the two transitions of the $q = 5$ clock model with cosine potential are of the KT-type, though there are no rigorous results. It is also assumed that the critical indices are the same as those in the Villain formulation.

The disagreement about the nature of the phase transitions stems from numerical results for the helicity modulus [80].

Most notably, Baek and Minnhagen [81] claim that since the helicity modulus does not vanish in the high-temperature phase, the upper transition is not of the KT-type.

It was shown by Kumano et al. in [82], however, that the definition used by Baek and Minnhagen is not suitable for systems with a discrete symmetry. The correct discrete definition yields the expected result, namely that the helicity modulus does vanish and the three-phase KT-picture holds.

The conclusion of Kumano et al, which was obtained by a Monte Carlo study, was verified by Chatelain [83] using the TMRG algorithm [38] (see also section 3.4). Chatelain also found that the critical indices match those of the Villain model (Eq. 8.4), implying the cosine model is in the same universality class.

After the rebuttal by Kumano et al., Baek et al. published another work [84] in which they again use the (in the eyes of Kumano et al.) wrong definition of the helicity modulus, yet calculated in a different way. Again they conclude the transition is not of the KT-type.

	T_1	T_2
Brito et al.[1] (2010) [86]	0.91	0.90
Borisenko et al. (2011) [85]	0.9056	0.9432
Kumano et al. (2013) [82]	0.908	0.944
Chatelain (2014) [83]	0.914	0.945
This work (finite-N scaling)	0.915	0.935
This work (finite-m scaling)	-	0.944

Table 8.1: Previous results for the transition temperatures for $q = 5$.

Meanwhile, Borisenko et al. [85] carried out a very detailed Monte Carlo study confirming the KT-picture, using Binder-cumulants to find the critical points and the magnetization and susceptability to find the critical indices.

Brito et al. [86] conclude from a Monte Carlo study that while the transition is of KT-type, the resolution of their numerical method is not high enough to distinguish between T_1 and T_2.

Table 8.1 shows the results for the transition temperatures found by other authors.

8.2.2 The $q = 6$ clock model

Here, there is overwhelming consensus that both transitions are of the KT-type. The only exceptions are Lapilli et al. [77] and Hwang [87].

Lapilli et al. use the incorrect definition of the helicity modulus.

Hwang asserts that the transition is not of KT-type because the data, which was obtained from systems of rather small size ($L \times L$-systems with $L = 20, \ldots, 28$), also agrees with a power-law divergence of the correlation length.

The previous results for the transition temperatures are listed in Table 8.2. For an overview that goes further back, see [68].

We note that [82, 86, 88] use Monte Carlo methods, while [68] uses the CTMRG algorithm (combined with finite-size scaling, but not with finite-m scaling).

[1] These authors found $T_1 > T_2$, which is not an error in the text, but due to the low resolution of the methods used.

[2] To obtain these values, the author assumed an algebraic divergence of the correlation length.

	T_1	T_2
Tomita and Okabe (2002) [88]	0.7014	0.9008
Hwang[2] (2009) [87]	0.632	0.997
Brito et al. (2010) [86]	0.68	0.90
Kumano et al. (2013) [82]	0.700	0.904
Krčmár et al. (2016) [68]	0.70	0.88
This work (finite-N scaling)	0.700	0.883
This work (finite-m scaling)	-	0.901

Table 8.2: Previous results for the transition temperatures for $q = 6$.

8.3 Spectrum of the corner transfer matrix

In order to get an idea of the accuracy that we might expect, we have plotted the spectrum of the $q = \{5, 6\}$ clock models in Fig. 8.1.

It is clear that the spectra of both clock models fall off at about the same pace, if we compare points in the ordered, massless and disordered phase. The $q = 6$ clock model has a slightly more degenerate spectrum, as might be expected from its larger symmetry group, but there is no clear pattern.

As compared to the Ising model (see section 3.7), the spectra of the $q = \{5, 6\}$ clock models fall off much more slowly[3]. This implies that a much larger bond dimension is needed to obtain the same accuracy for quantities in the thermodynamic limit.

8.4 Magnetization

For the clock model, we define the magnetization per site as

$$M = \langle \cos \theta_0 \rangle, \tag{8.6}$$

where θ_0 is the central spin.

[3]For the calculation of the spectrum of the Ising model in this work, a bond dimension of $m = 250$ was used, as opposed to $m = 100$ for the clock model. This means that, in small part, the slower decay of the spectrum is due to the normalization $\mathrm{Tr}\, A^4 = 1$. But this does not change the general picture that the spectra of the $q = \{5, 6\}$ clock models decay more slowly.

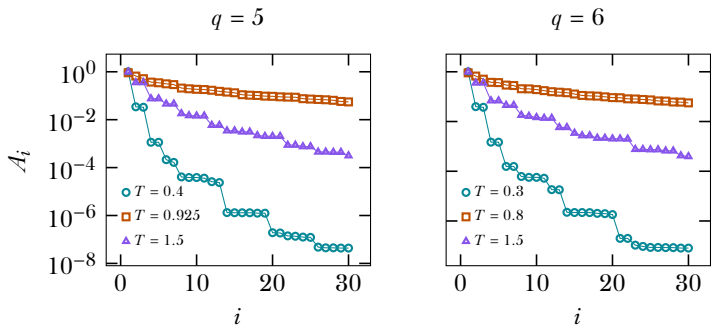

Figure 8.1: First part of the spectrum of A with fixed boundary, calculated with $m = 100$ and a convergence threshold of 10^{-8}, at temperatures corresponding to the ordered phase, approximate midpoint of the massless phase and disordered phase, respectively.

This quantity can be computed in the same way as for the Ising model (see section 3.6.2) by generalizing the tensor b_{ijkl} to

$$b_{ijkl} = \sum_{n\in\{0,\dots,q-1\}} \cos\left(\frac{2\pi n}{q}\right) \delta_{nijkl}. \tag{8.7}$$

8.5 Classical analogue to the entanglement entropy

The classical analogue to the half-chain entanglement entropy S is defined in section 3.6.3. Its definition remains valid.

In the limit $T \to \infty$, for both a fixed and free boundary, we have

$$S(T \to \infty) = 0. \tag{8.8}$$

To see this, consider that all 2^{2N} configurations on the inner edges of the $N \times N$ quadrant represented by the corner transfer matrix are equally likely in this limit, hence

$$A_{ij} = \frac{1}{2^{2N}}, \tag{8.9}$$

which has one eigenvalue of 1 and the others 0[4].

In the limit $T \to 0$, there is only one non-zero matrix element in the case of a fixed boundary (namely all inner spins having the same value as the outer boundary), and q equally likely configurations in the case of a free boundary, yielding

$$S^{\text{fixed}}(T = 0) = 0,$$
$$S^{\text{free}}(T = 0) = \log q.$$

For a fixed boundary, the point of maximum entropy approaches the massless phase from the high-temperature region, hence tending towards T_2. In contrast, the point of maximum entropy approaches T_1 for systems with a free boundary.

Fig. 8.2 and Fig. 8.3 show these quantities for $q = 5$ and $q = 6$ for systems with a fixed boundary, clearly confirming the three-phase picture.

8.6 Transition temperatures

Since we expect an essential singularity of the form in Eq. 8.1 for both transitions, for finite systems we have

$$N = a \exp\left(b|T^\star(N) - T_c|^{-1/2}\right), \tag{8.10}$$

where N is an effective finite length scale of the system and a and b are non-universal constants.

N is the system size in the case of finite-size scaling and a length scale derived $\xi(m)$ from the bond dimension m in the case of finite-m scaling. Throughout this chapter, we have defined $\xi(m)$ through the relation

$$S \propto \frac{c}{6} \log \xi(m) \tag{8.11}$$

where $c = 1$ is expected, since the massless phase corresponds to a Gaussian model [70]. These assumptions are validated in section 8.7.1.

We define $T^\star(N)$ as the point of maximum entanglement entropy, as discussed in section 5.4.

[4] One can also make the argument that the corresponding quantum state tends to a product state in the limit $T \to 0$, yielding the same conclusion.

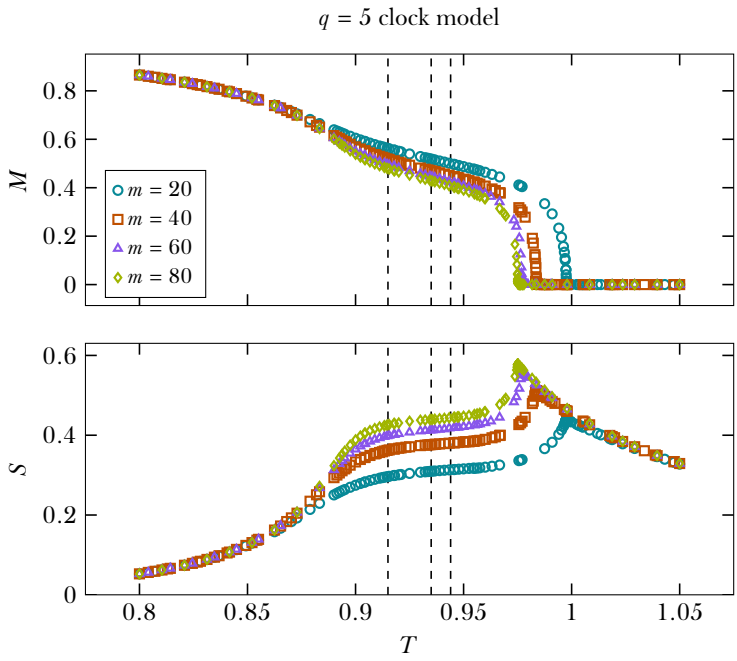

Figure 8.2: Classical analogue to half chain entanglement entropy (section 3.6.3) and magnetization (Eq. 8.6) computed for systems with a fixed boundary for the $q = 5$ clock model. Simulations were done with a convergence threshold of 10^{-7}. The dashed lines denote the transition temperatures found in this study.

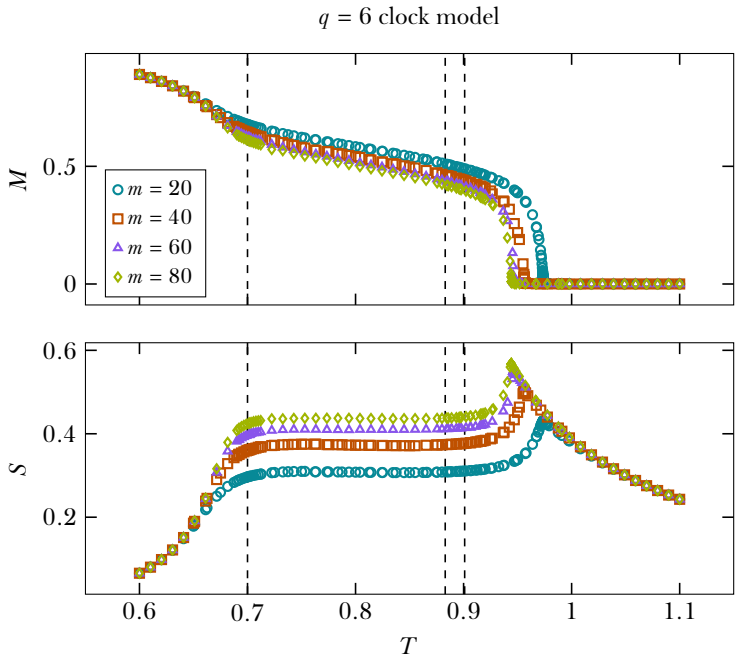

Figure 8.3: Classical analogue to half chain entanglement entropy (section 3.6.3) and magnetization (Eq. 8.6) computed for systems with a fixed boundary for the $q = 6$ clock model. Simulations were done with a convergence threshold of 10^{-7}. The dashed lines denote the transition temperatures found in this study.

Inverting Eq. 8.10 gives the following relations for the pseudocritical transition temperatures

$$T_1^\star(N) = -\frac{\alpha_1}{(\log \beta_1 N)^2} + T_1 \tag{8.12}$$

$$T_2^\star(N) = \frac{\alpha_2}{(\log \beta_2 N)^2} + T_2 \tag{8.13}$$

where $\alpha = b^2$ and $\beta = 1/a$ (we drop the subscripts denoting the transition).

For convenience, we define the scaled length variable

$$\ell = (\log \beta N)^2, \tag{8.14}$$

such that

$$T^\star(N) - T_c \propto \frac{1}{\ell}. \tag{8.15}$$

8.6.1 Numerical difficulties with finite-m simulations around T_1

For both the $q = \{5, 6\}$ clock models, it has been found that locating $T_1^\star(m)$ is not possible, since for systems with a free boundary, numerical errors cause the matrices A and P to lose their symmetry and converge to a fixed boundary fixed point instead. This happens after a modest amount of steps, especially near $T_1(m)^\star$, making it impossible to reach any feasible convergence threshold such as 10^{-6}.

This means that for locating T_1, we must rely on finite-size scaling, whereas for locating T_2 we can rely on both finite-size and finite-m scaling.

8.6.2 Transition from the ordered to the massless phase T_1

Fig. 8.4 and Fig. 8.5 show the fits to Eq. 8.10 for $q = \{5, 6\}$, yielding

$$T_1^{q=5} = 0.915, \qquad T_1^{q=6} = 0.700. \tag{8.16}$$

Conform to the Kosterlitz-Thouless divergence of the correlation length, the pseudocritical temperatures indeed become linear in $\frac{1}{\ell}$, with ℓ defined in Eq. 8.14.

It is interesting to note that finite-size effects are much more pronounced for $q = 5$.

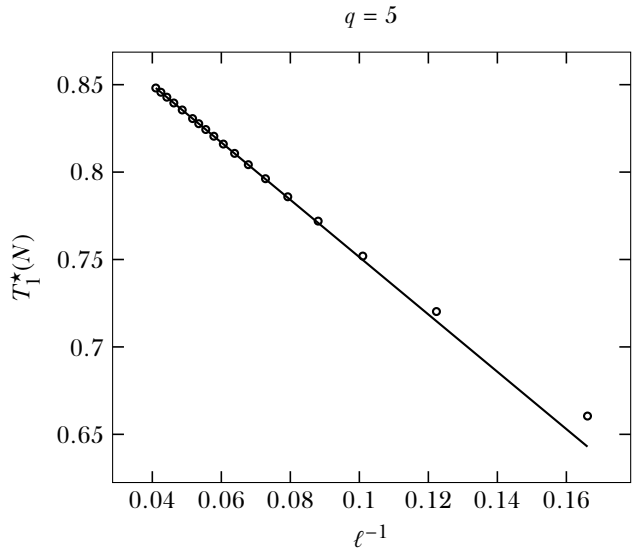

Figure 8.4: We find $T_1 = 0.915$ for the $q = 5$ clock model. We have fitted the final 8 points $n = \{60, 65, 70, 80, 90, 100, 110, 120\}$. Not included in the fit are $n = \{10, 15, \ldots, 55\}$. m was chosen such that the truncation error was smaller than 10^{-6} for $n \leq 70$ and smaller than 10^{-5} for $n > 70$. In finding the maximum of the entropy, a tolerance in temperature of 10^{-5} was used.

8.6.3 Transition from the massless to the disordered phase T_2

8.6.3.1 Finite-size scaling

Finite-size scaling, shown in Fig. 8.6 for $q = 5$ and Fig. 8.8 for $q = 6$ yields

$$T_2^{q=5} = 0.935, \qquad T_2^{q=6} = 0.883. \tag{8.17}$$

For both clock models, finite-size effects are large. For $q = 6$, the finite-size effects are more pronounced than at T_1.

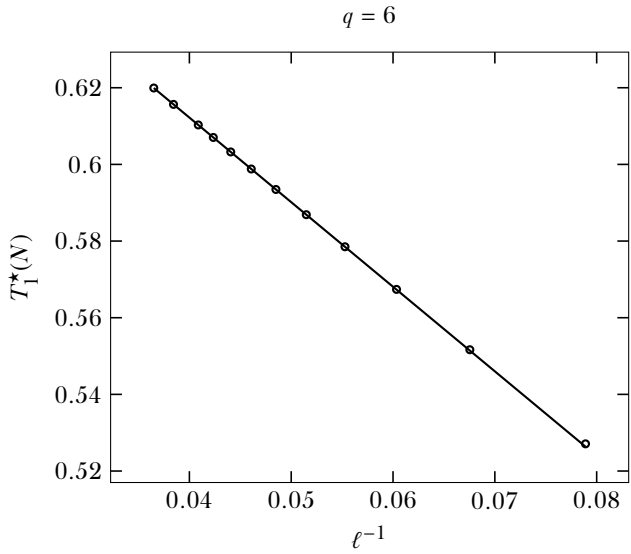

Figure 8.5: We find $T_1 = 0.700$ for the $q = 6$ clock model. We have fitted the final 8 points $n = \{35, 40, 45, 50, 55, 60, 70, 80\}$. Not included in the fit are $n = \{15, 20, 25, 30\}$. m was chosen such that the truncation error was smaller than 10^{-6} for $n \leq 60$ and smaller than 10^{-5} for $n > 60$. In finding the maximum of the entropy, a tolerance in temperature of 10^{-5} was used.

8.6.3.2 Finite-m scaling

Finite-m scaling, shown in Fig. 8.10 for $q = 5$ and Fig. 8.9 for $q = 6$ yields

$$T_2^{q=5} = 0.944, \qquad T_2^{q=6} = 0.901. \tag{8.18}$$

It is seen that with finite-m simulations, systems of significantly larger effective size can be simulated. From the finite-size fits to $T_2^\star(N)$, it can be estimated that a system of $m = 90$ approximately corresponds to a 2700×2700 lattice for $q = 5$ and a 2400×2400 lattice for $q = 6$.

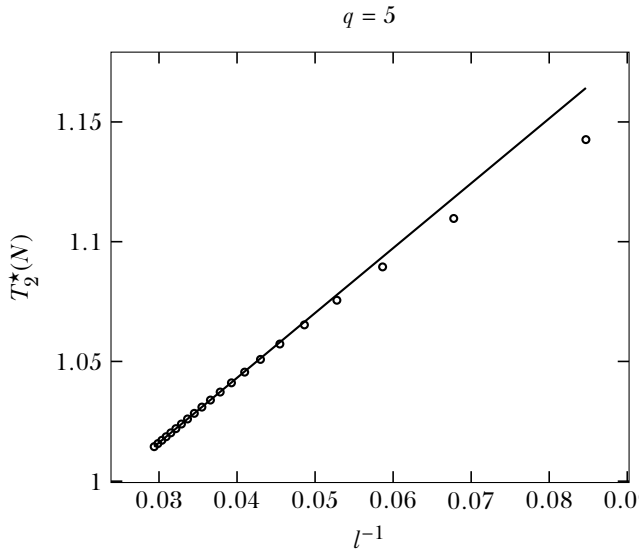

Figure 8.6: We find $T_2 = 0.935$ for the $q = 5$ clock model with finite-size scaling. We have fitted the final 6 points $n = \{85, 90, \ldots, 110\}$. m was chosen such that the truncation error was smaller than 10^{-6}. In finding the maximum of the entropy, a tolerance in temperature of 10^{-6} was used.

There is some structure in the data, but as long as a wide range of m values is included, the estimation of T_2 is robust.

8.7 The massless phase

8.7.1 Central charge

By fitting the relation in Eq. 8.11, where $\xi(m)$ is calculated as in section 5.2, we can directly extract the central charge of the massless phase.

For $q = \{5, 6\}$ the results are shown in the top panels of Fig. 8.11 and Fig. 8.12. For both models, we recover $c = 1$.

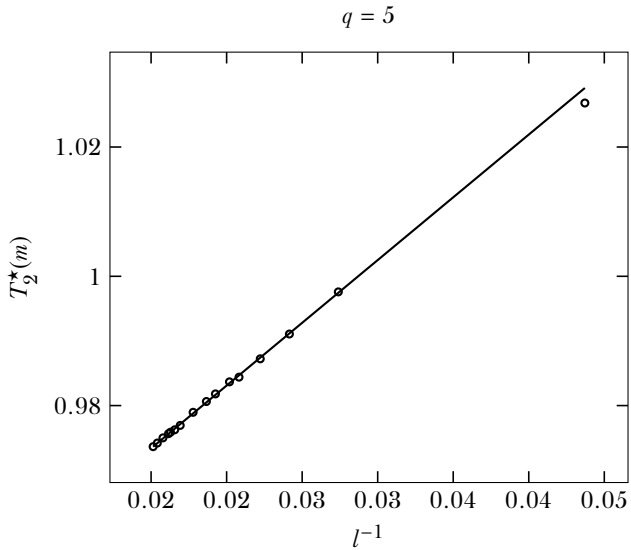

Figure 8.7: For the finite-m simulations, the fit yields $T_2 = 0.944.$ using $m = 20, 25, \ldots, 90$ with a convergence threshold of 10^{-7}. The pseudocritical temperature belonging to $m = 10$ is also shown, but is not included in the fit.

For $q = 5$, the positions of T_1 and T_2 do not precisely agree with the region in which a good fit to Eq. 8.11 can be obtained. The actual massless phase seems to be larger than what the critical temperatures indicate.

However, it is not clear how an effective value of c diverges from 1 outside the massless phase, so we do not draw any conclusions about the correctness of T_1 and T_2 for $q = 5$ based on these results.

8.7.2 Varying exponent for the magnetization

We may verify the exponent with which the magnetization goes to zero in the massless phase by fitting

$$M(m, T) = \xi(m)^{-\frac{\eta(T)}{2}}, \tag{8.19}$$

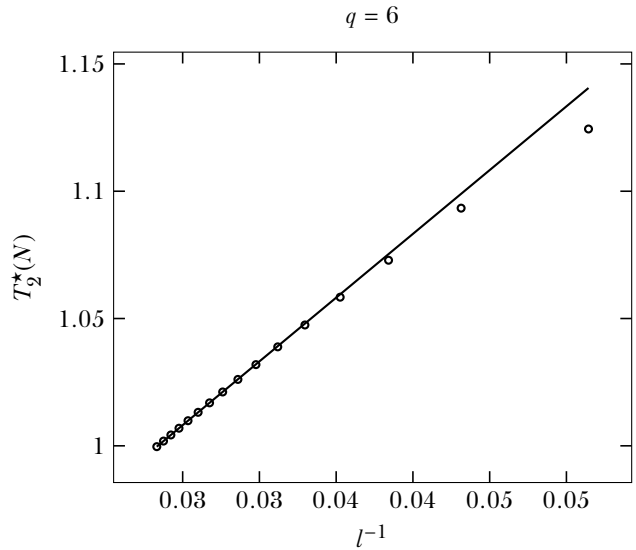

Figure 8.8: We find $T_2 = 0.883$ for the $q = 6$ clock model with finite-size scaling. We have fitted the final 6 points $n = \{60, 65, \ldots, 85\}$. The points $n = \{10, 15, \ldots, 55\}$ were not included. m was chosen such that the truncation error was smaller than 10^{-6}. In finding the maximum of the entropy, a tolerance in temperature of 10^{-6} was used.

with $\xi(m)$ again defined via Eq. 8.11.

The result is shown in the middle panels of Fig. 8.11 and Fig. 8.12 for $q = \{5, 6\}$, respectively.

If we assume that the model under study is in the same universality class as the Villain formulation, η should take the values listed in Eq. 8.4 at the critical points. Again, the positions of the critical points found in this work seem to be too close together, except for the lower transition of $q = 6$, which agrees well with the theoretical value.

Since the lower transition for $q = 6$ suffers the least from finite-size effects, it is plausible that the disagreement between the other transitions and the value

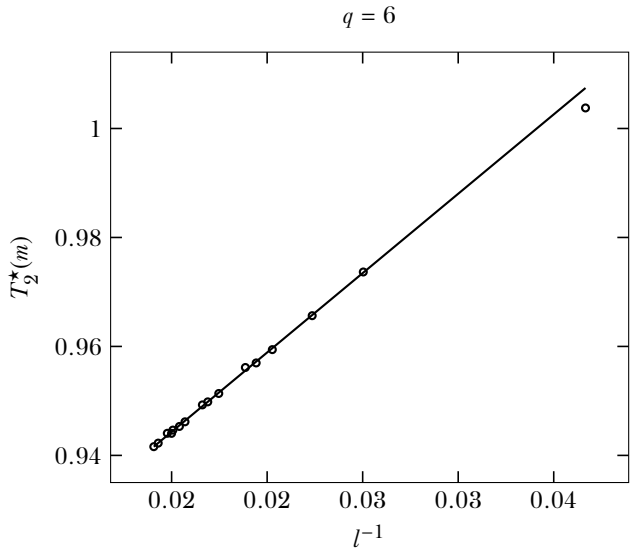

Figure 8.9: For the finite-m simulations, the fit yields $T_2 = 0.901.$ using $m = 20, 25, \ldots, 90$ with a convergence threshold of 10^{-7}. The pseudocritical temperature belonging to $m = 10$ is also shown, but is not included in the fit.

of η will be resolved when larger systems are considered, or finite-size effects are properly taken into account. We come back to this point in the discussion.

The lower panels of Fig. 8.11 and Fig. 8.12 show the norm of residuals of the fit to Eq. 8.19. For $q = 6$, there were values of the magnetization for $0.7 < T < 0.83$ that were lower than expected for certain values of m, reflected by the higher norm of residuals in this region. This did not significantly influence the values of c and η found.

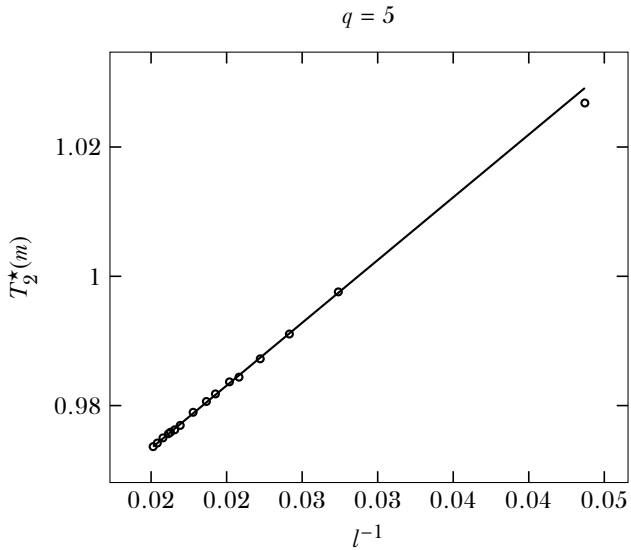

Figure 8.10: For the finite-m simulations, the fit yields $T_2 = 0.944.$ using $m = 20, 25, \ldots, 90$ with a convergence threshold of 10^{-7}. The pseudocritical temperature belonging to $m = 10$ is also shown, but is not included in the fit.

8.8 Discussion

8.8.1 Finite-size effects

Overall, the values of T_1 and T_2 for $q = \{5, 6\}$ in this work agree reasonably well with the values found by other authors, see Table 8.1 and Table 8.2.

Finite-size scaling within the CTMRG suffers more from finite-size effects than finite-m scaling does, since with finite-size simulations smaller system sizes can be reached.

It is plausible that this is the reason that finite-size scaling yields values of the critical temperatures that differ somewhat from previous results and the results of finite-m scaling.

The discussion in section 7.4.1 for the Ising model is applicable here as

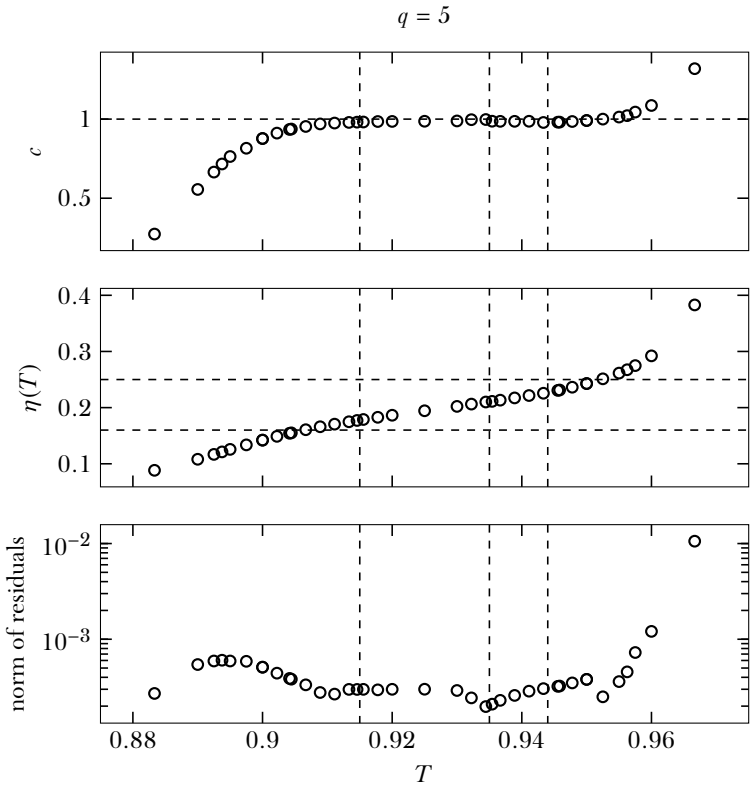

Figure 8.11: Top panel: central charge obtained from fit to Eq. 8.11. The horizontal dashed line marks $c = 1$. Middle panel: $\eta = 2\beta/\nu$ obtained from fit to Eq. 8.19. First 4 values were left out of the fit. The horizontal dashed lines mark $\eta = 4/25$ and $\eta = 1/4$, the exact values obtained in the Villain formulation. Bottom panel: norm of residuals for the fit to Eq. 8.19. For all calculations, we have used $m = 10, 20, \ldots, 100$, simulated with a convergence threshold of 5×10^{-8}. The first four values of m were left out of the fits to mitigate finite-size effects. The vertical dashed lines mark the values of the critical points found in this work, where both results of T_2 are included.

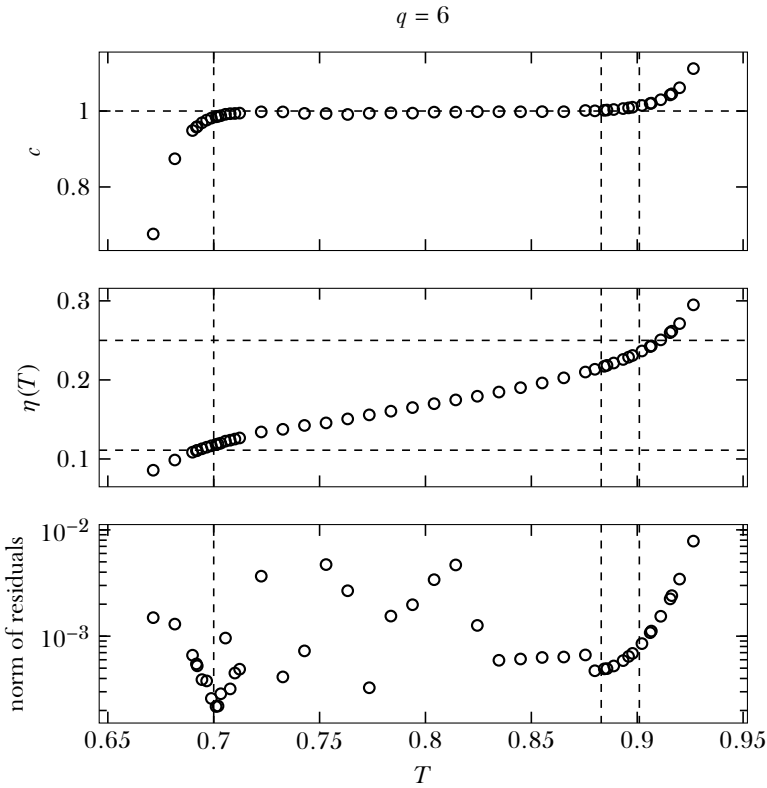

Figure 8.12: Same as Fig. 8.11, except that in the middle panel, the horizontal lines mark $\eta = 4/36$ and $\eta = 1/4$. Finite-size effects were less prominent, but there were some anomalous simulations for $0.7 < T < 0.83$ that showed lower magnetization than expected for certain m-values. We have found that including every m-value in the fit gave the best results.

well. In summary, the most straightforward way of improving finite-size results is to include finite-size corrections, which should be feasible since the data is of high quality. In conjunction with this, a more systematic study of the convergence of quantities and the location of the pseudocritical points (extending results in section 6.3.2) may reveal that simulating larger system sizes is in fact possible without too much loss of accuracy.

For finite-m scaling, inherent deviations from the basic scaling laws, stemming from the underlying CTM spectrum, make including finite-size corrections less feasible. Using m-values that are far apart or that are specifically selected to mitigate the effects of the half-moon patterns may yield better results.

Results for the exponent η indicate that the critical temperatures found in both this study and previous work might be too close together. It is conceivable that, after considering larger systems and taking into account finite-size corrections, both critical temperatures and the values of η will be adjusted outwards towards their true values, thereby completely reconciling the results.

8.8.2 Other means of studying the transitions T_1 and T_2

In this study, we have used the point of maximum entanglement entropy as a definition of the pseudocritical point. The most obvious drawback of this method is that locating T_1 is not possible with finite-m simulations, as described in section 8.6.1. Finite-size simulations near T_1 are possible, but costly, since the spectrum of the corner transfer matrix decays slowly for systems with a free boundary.

A different way of finding T_1 is through the higher order parameters

$$M_a = \langle e^{ia\theta_0} \rangle, \tag{8.20}$$

which should obey

$$|M_a| \propto \exp\left(-Ca^2/(T_1 - T)^{1/2}\right), \tag{8.21}$$

with C a non-universal constant [74].

M_a is readily obtainable with the CTMRG method and does not require a free boundary. However, it is not clear if this will increase the precision of T_1.

The transition T_2 may also be found by studying the magnetic susceptibility, as was done by [85]. The susceptibility diverges more strongly than the entropy, but requires numerical derivatives to find. It is plausible that this

method would not yield a better accuracy than current method, since it requires the same simulations to obtain T_2. Nonetheless, it would serve as a good consistency check.

Finally, we note that it is possible to introduce the spin-flip symmetry of the Hamiltonian on the tensor level, demonstrated in [89] for the two-dimensional quantum case. This would allow for the studying of T_1 with finite-m approximations.

9
Conclusions

In this thesis, we investigated finite bond dimension scaling with the corner transfer matrix renormalization group (CTMRG) method for two-dimensional classical models. The two main questions posed at the outset were

(i) how finite bond dimension scaling works within the CTMRG method and relatedly, how it compares to finite-size scaling within the same method, and

(ii) how finite bond dimension scaling with CTMRG compares to other numerical approaches in a difficult scenario.

To address (i), we studied the square-lattice Ising model in Chap. 7. It is shown that exponents and the transition temperature may be approximated with a scaling analysis in the correlation length defined in terms of the row-to-row transfer matrix at the (pseudo)critical point, as was suggested by [7]. However, the calculated quantities show inherent deviations from the basic scaling laws, due to the spectrum of the underlying corner transfer matrix (CTM). These deviations are mitigated to some extent when we define the correlation length in terms of the classical analogue of the entanglement entropy. Scaling directly in the bond dimension m is also possible, but less accurate since the law for the correlation length

$$\xi \propto m^{\kappa}$$

holds only in the limit $m \to \infty$ and does not take into account the spectrum of the CTM that is obtained. Our results indicate that κ is between 1.93 and 1.96, while a theoretical analysis [30] predicts $\kappa \approx 2.03$, but the discrepancy can be explained by finite-m effects and low quality of the fit because of deviations due to the CTM spectrum.

It was found that finite-m scaling and finite-size scaling yield comparable accuracy for critical exponents and the transition temperature. With finite-m

scaling larger effective system sizes are obtainable, but finite-size approximations do not suffer from the deviations due to the CTM spectrum and are consequently of higher quality. Therefore it is plausible that finite-size results will improve significantly if corrections to scaling are included in the fits.

In Chap. 6, the convergence properties of both finite-m and finite-size calculations were studied. For finite-size simulations, it is not entirely clear how the chosen bond dimension (and correspondingly, the truncation error) influences the precision of quantities and the position of the pseudocritical point. It might be possible to simulate larger system sizes without much loss of accuracy, but it seems unlikely that the same system sizes as in the finite-m regime are accessible. For finite-m results it is much easier to assess the convergence of quantities. The quality of the fit remains limited by the structure that is inherent in the data.

To compare finite bond dimension scaling with CTMRG to other numerical approaches (ii), we studied the two phase transitions of the clock model with $q = \{5, 6\}$ states in Chap. 8. This model is subject to some controversy, because while the renormalization group analysis suggests that the transitions are of the Kosterlitz-Thouless (KT) type, recent papers claim that this may not be the case.

We find a divergence of the correlation length that is consistent with the KT picture. Furthermore, we find a varying value for the correlator exponent η that comes close to exact values for the model in the Villain formulation, which has two KT transitions. From this, we conclude that it is very implausible that the phase diagram found from the renormalization group analysis needs to be altered.

The values that we found for T_1 and T_2 for $q = \{5, 6\}$ agree reasonably well with the values found by other authors. We were able to study T_1 only with finite-size scaling, since it requires approximating systems with a free boundary, which is not possible near T_1 due to numerical instability of the tensors in finite-m approximations.

Finite-size scaling within the CTMRG suffers more from finite-size effects than finite-m scaling does, since with finite-size simulations smaller system sizes are obtainable. It is plausible that this is the reason that finite-size scaling yields values of the critical temperatures that differ somewhat from previous results and the results of finite-m scaling.

The remarks made for the Ising model are applicable here as well. In summary, the most straightforward way of improving finite-size results is to include finite-size corrections, which should be feasible since the data is of high quality. In conjunction with this, a more systematic study of the convergence of quantities and the location of the pseudocritical points may reveal that sim-

ulating larger system sizes is in fact possible without too much loss of accuracy. For finite-m scaling, inherent deviations from the basic scaling laws, stemming from the underlying CTM spectrum, make including finite-size corrections less feasible.

Results for the exponent η indicate that the critical temperatures found in both this study and previous work might be too close together. It is conceivable that, after considering larger systems and taking into account finite-size corrections, both critical temperatures and the values of η will be adjusted outwards towards their true values, thereby completely reconciling the results.

Overall, we conclude that finite-m scaling is a valuable alternative to finite-size scaling within CTMRG, since larger system sizes are accessible. The CTMRG analysis is itself a valuable addition to other approximation methods such as Monte Carlo, yielding comparable results, while establishing the KT picture from completely different principles. Furthermore it reveals information, such as the the spectrum of the transfer matrices and the central charge of the massless phase, that is not accessible otherwise.

Apart from the possibilities for improvement already mentioned, it is useful to consider the application of the methods in this thesis to two-dimensional quantum and three-dimensional classical systems. The idea of generalizing the CTM approach to three dimensions was not lost on Baxter [15, p. 401] and was later attempted by Nishino and Okunishi [90].

For two-dimensional quantum systems, iPEPS [28] is a wave function ansatz for translationally invariant systems in the thermodynamic limit. It is the natural extension of the matrix-product state (MPS) ansatz to two dimensions. Optimizing the wave function or computing observables requires contraction of a tensor network that is similar to the one used in this thesis to approximate the partition function of two-dimensional classical models. This has in fact been done using the CTM approach [91]. The differences with the two-dimensional classical case are that the site-tensors are themselves approximations of the optimal tensors within the ansatz and that, since the iPEPS ansatz works directly in the thermodynamic limit, there is no concept of a physical boundary or finite-size scaling. Hence, finite bond dimension scaling may be the only method to systematically analyze the effect of the approximations made.

A
Correspondence of quantum and classical lattice systems

The partition function of a discrete quantum mechanical system is given by

$$Z_q = \mathrm{Tr}\exp(-\beta H_q) = \sum_\sigma \langle\sigma|\exp(-\beta H_q)|\sigma\rangle \tag{A.1}$$

Imagine splitting the imaginary time interval β into N small steps:

$$\beta = N\delta\tau, \tag{A.2}$$

$$\exp(-\beta H_q) = \exp(-\delta\tau H_q)^N. \tag{A.3}$$

Recall that for any orthonormal basis, the identity can be expressed as a sum over projectors onto the basis states

$$\mathbb{1} = \sum_\sigma |\sigma\rangle\langle\sigma|. \tag{A.4}$$

If we insert $N-1$ resolutions of indentity into Eq. A.1, we obtain

$$Z_q = \sum_\sigma \sum_{\sigma_1,\ldots,\sigma_{N-1}} \langle\sigma|\exp(-H_q\delta\tau)|\sigma_1\rangle\ldots\langle\sigma_{N-1}|\exp(-H_q\delta\tau)|\sigma\rangle. \tag{A.5}$$

This is the imaginary time path integral formulation of quantum mechanics[1]. Similar to the real-time path integral, an evolution in the imaginary time direction is expressed as a sum over all paths connecting the initial and final state, which are the same here, since we are taking the trace.

[1] This formulation of Z_q is central to quantum Monte Carlo methods, which regard $\langle\sigma|\exp(-H_q\delta\tau)|\sigma_1\rangle\ldots\langle\sigma_{N-1}|\exp(-H_q\delta\tau)|\sigma\rangle$ as the Boltzmann weights of a corresponding classical system with an additional dimension. These weights can become negative for certain frustrated or fermionic systems, leading to the famous negative sign problem [6].

We turn to the partition function of a classical system, written as a product of its transfer matrix, as in Eq. 3.11:

$$Z_{\mathrm{cl}} = \mathrm{Tr}\, T^N. \tag{A.6}$$

There is a striking similarity between a quantum mechanical partition function in d dimensions and a classical partition function in $d + 1$ dimensions. Adding a row to the classical lattice by applying the transfer matrix corresponds to time evolution of a quantum system:

$$T \longleftrightarrow \exp(-\delta\tau H_q) \approx 1 - H_q \delta\tau. \tag{A.7}$$

The classical temperature corresponds to the coupling constants in the Hamiltonian H_{q}. Letting $\beta \to \infty$ (or equivalently $T \to 0$) amounts to taking $N \to \infty$, while keeping $\delta\tau$ fixed. In this limit, analogously to the transfer matrix for the classical system (see Eq. 3.19), the operator $\exp(-\beta H_{\mathrm{q}})$ becomes a projector onto the ground state. Thus, a quantum lattice in the ground state corresponds to a classical lattice that is infinite in its additional dimension.

For some examples of mappings between quantum and classical models, see [92], which also contains some comments on the validity of the reverse mapping (classical to quantum). For a rigorous treatment on the equivalence between d-dimensional quantum Ising model with transverse field and $(d+1)$-dimensional classical Ising model, see [93].

B
Introduction to tensor networks

This appendix discusses only what is strictly necessary to understand the tensor network notation in this thesis. For a more comprehensive introduction, see [24].

B.1 Tensors, or multidimensional arrays

In the field of tensor networks, a tensor is a multidimensional table with numbers – a convenient way to organize information. It is the generalization of a vector

$$v_i = \begin{bmatrix} v_1 \\ \vdots \\ v_n \end{bmatrix}, \tag{B.1}$$

which has one index, and a matrix

$$M_{ij} = \begin{bmatrix} M_{11} & \dots & M_{1n} \\ \vdots & & \vdots \\ M_{m1} & \dots & M_{mn} \end{bmatrix}, \tag{B.2}$$

which has two. A tensor of rank N has N indices:[1]

$$T_{i_1 \dots i_N}. \tag{B.3}$$

A tensor of rank zero is just a scalar.

[1] The definition of rank in this context is not to be confused with the rank of a matrix, which is the number of linearly independent columns. Synonyms of tensor rank are tensor degree and tensor order.

B.2 Tensor contraction

Tensor contraction is the higher-dimensional generalization of the dot product

$$\boldsymbol{a} \cdot \boldsymbol{b} = \sum_i a_i b_i, \tag{B.4}$$

where a lower-dimensional tensor (in this case, a scalar, which is a zero-dimensional tensor) is obtained by summing over all values of a repeated index.

Examples are matrix-vector multiplication

$$(M\boldsymbol{a})_i = \sum_j M_{ij} a_j, \tag{B.5}$$

and matrix-matrix multiplication

$$(AB)_{ij} = \sum_k A_{ik} B_{kj}, \tag{B.6}$$

but a more elaborate tensor multiplication could look like

$$w_{abc} = \sum_{d,e,f} T_{abcdef} v_{def}. \tag{B.7}$$

As with the dot product between vectors, matrix-vector multiplication and matrix-matrix multiplication, a contraction between tensors is only defined if the dimensions of the indices match.

B.3 Tensor networks

A tensor network is specified by a set of tensors, together with a set of contractions to be performed. For example:

$$M_{ab} = \sum_{i,j,k} A_{ai} B_{ij} C_{jk} D_{kb}, \tag{B.8}$$

which corresponds to the matrix product $ABCD$.

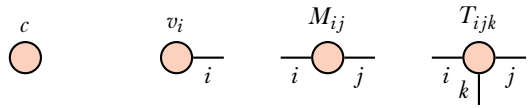

Figure B.1: Open-ended lines, called legs, represent unsummed indices. A tensor with no open legs is a scalar.

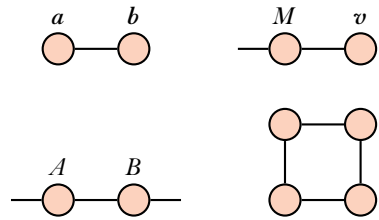

Figure B.2: Connected legs represent contracted indices. The networks in the figure represent $\sum_i a_i b_i$ (dot product), $\sum_j M_{ij} a_j$ (matrix-vector product), $\sum_k A_{ik} B_{kj}$ (matrix-matrix product) and $\mathrm{Tr}\, ABCD$, respectively.

B.3.1 Graphical notation

It is highly convenient to introduce a graphical notation that is common in the tensor network community. It greatly simplifies expressions and makes certain properties manifest.

Each tensor is represented by a shape. Open-ended lines, called legs, represent unsummed indices. See Fig. B.1. If it clear from the context, index labels may be omitted from the open legs.

Each contracted index is represented by a connected line. See Fig. B.2.

Many tensor equations, while burdensome when written out, are readily understood in this graphical way. As an example, consider the matrix trace in Fig. B.2, where its cyclic property is manifest.

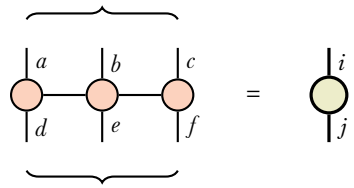

Figure B.3: Reshaping a tensor T_{abcdef} to T_{ij}

B.3.2 Reshaping tensors

Several indices can be taken together to form a single, joint index, that runs over all combinations of the indices that fused into it. For example, an $m \times n$ matrix can be reshaped into an mn vector.

$$M_{ij} = v_a \qquad a \in \{1, \ldots, mn\}. \tag{B.9}$$

Some convention has to be chosen to map the joint index i, j onto the single index a, for example

$$a = (n-1)i + j, \tag{B.10}$$

which orders the indices of the matrix M row by row

$$11, 12, \ldots, 1n, 21, 22, \ldots, mn-1, mn. \tag{B.11}$$

Graphically, an index contraction is represented as a bundling of the open legs of a tensor network. See Fig. B.3 for an example.

B.3.3 Computational complexity of contraction

A contraction between two tensors

$$C_{a_1 \ldots a_m b_1 \ldots b_n} = \sum_z A_{a_1 \ldots a_m z} B_{z b_1 \ldots b_n} \tag{B.12}$$

takes

$$\mathcal{O}\left(|z| \prod_i |a_i| \prod_i |b_i|\right) \tag{B.13}$$

operations, where $|i|$ is the dimension of index i. This is a straightforward generalisation of the fact that multiplication of an $n \times m$-matrix and an $m \times p$-matrix takes $\mathcal{O}(nmp)$ operations.

This implies that the complexity of contracting an entire network of tensors depends vitally on the order in which the indices are summed over (in which order the "legs are closed"). For a simple example of this, see section 4.2.1 of [94].

Determining the optimal order is highly non-trivial (in fact, known to be NP-hard) and also depends on available computer memory [95].

Bibliography

[1] R. J. Baxter, "Variational approximations for square lattice models in statistical mechanics", Journal of Statistical Physics **19**, 461–478 (1978).

[2] R. J. Baxter, *Exactly solved models in statistical mechanics* (Elsevier, 1982) Chap. 13.

[3] S. K. Tsang, "Square lattice variational approximations applied to the Ising model", Journal of Statistical Physics **20**, 95–114 (1979).

[4] T. Nishino, and K. Okunishi, "Corner transfer matrix renormalization group method", Journal of the Physical Society of Japan **65**, 891–894 (1996).

[5] S. R. White, "Density matrix formulation for quantum renormalization groups", Physical Review Letters **69**, 2863 (1992).

[6] M. Troyer, and U. Wiese, "Computational complexity and fundamental limitations to fermionic quantum Monte Carlo simulations", Physical Review Letters **94**, 170201 (2005).

[7] T. Nishino, K. Okunishi, and M. Kikuchi, "Numerical renormalization group at criticality", Physics Letters A **213**, 69–72 (1996).

[8] L. P. Kadanoff, "More is the same; phase transitions and mean field theories", Journal of Statistical Physics **137**, 777 (2009).

[9] C. Domb, *The critical point: a historical introduction to the modern theory of critical phenomena* (CRC Press, 1996).

[10] R. Peierls, "On Ising's model of ferromagnetism", Mathematical Proceedings of the Cambridge Philosophical Society **32**, 477–481 (1936).

[11] L. Onsager, "Crystal statistics. I. a two-dimensional model with an order-disorder transition", Phys. Rev. **65**, 117–149 (1944).

[12] T. H. Berlin, and M. Kac, "The spherical model of a ferromagnet", Physical Review **86**, 821–835 (1952).

[13] B. Sutherland, C. N. Yang, and C. P. Yang, "Exact solution of a model of two-dimensional ferroelectrics in an arbitrary external electric field", Physical Review Letters **19**, 588–591 (1967).

[14] R. J. Baxter, "Eight-vertex model in lattice statistics", Physical Review Letters **26**, 832–833 (1971).

[15] R. J. Baxter, *Exactly solved models in statistical mechanics* (Elsevier, 1982).

[16] H. A. Kramers, and G. H. Wannier, "Statistics of the two-dimensional ferromagnet. Part II", Phys. Rev. **60**, 263–276 (1941).

[17] R. B. Griffiths, "Dependence of critical indices on a parameter", Physical Review Letters **24**, 1479–1482 (1970).

[18] M. E. Fisher, "Quantum corrections to critical-point behavior", Physical Review Letters **16**, 11–14 (1966).

[19] R. J. Baxter, "Dimers on a rectangular lattice", Journal of Mathematical Physics **9**, 650–654 (1968).

[20] S. Östlund, and S. Rommer, "Thermodynamic limit of density matrix renormalization", Physical Review Letters **75**, 3537 (1995).

[21] S. Rommer, and S. Östlund, "Class of ansatz wave functions for one-dimensional spin systems and their relation to the density matrix renormalization group", Physical Review B **55**, 2164 (1997).

[22] M. P. Nightingale, and H. W. J. Blöte, "Gap of the linear spin-1 Heisenberg antiferromagnet: a Monte Carlo calculation", Physical Review B **33**, 659–661 (1986).

[23] P. Calabrese, and J. Cardy, "Entanglement entropy and quantum field theory", Journal of Statistical Mechanics: Theory and Experiment **2004**, P06002 (2004).

[24] R. Orús, "A practical introduction to tensor networks: matrix product states and projected entangled pair states", Annals of Physics **349**, 117–158 (2014).

[25] G. Vidal, "Entanglement renormalization", Physical Review Letters **99**, 220405 (2007).

[26] F. Verstraete, and J. I. Cirac, "Renormalization algorithms for quantum-many body systems in two and higher dimensions", arXiv cond-mat/0407066 (2004).

[27] G. Vidal, "Classical simulation of infinite-size quantum lattice systems in one spatial dimension", Physical Review Letters **98**, 070201 (2007).

[28] J. Jordan, R. Orús, G. Vidal, F. Verstraete, and J. I. Cirac, "Classical simulation of infinite-size quantum lattice systems in two spatial dimensions", Physical Review Letters **101**, 250602 (2008).

[29] L. Tagliacozzo, T. R. De Oliveira, S. Iblisdir, and J. I. Latorre, "Scaling of entanglement support for matrix product states", Physical Review B **78**, 024410 (2008).

[30] F. Pollmann, S. Mukerjee, A. M. Turner, and J. E. Moore, "Theory of finite-entanglement scaling at one-dimensional quantum critical points", Physical Review Letters **102**, 255701 (2009).

[31] K. G. Wilson, "The renormalization group: critical phenomena and the Kondo problem", Reviews of Modern Physics **47**, 773 (1975).

[32] D. Poulin, A. Qarry, R. Somma, and F. Verstraete, "Quantum simulation of time-dependent Hamiltonians and the convenient illusion of Hilbert space", Physical Review Letters **106**, 170501 (2011).

[33] S. R. White, and R. M. Noack, "Real-space quantum renormalization groups", Physical Review Letters **68**, 3487 (1992).

[34] R. M. Noack, and S. R. White, "The density matrix renormalization group", in *Density-matrix renormalization, a new numerical method in physics*, Vol. 528, edited by I. Peschel, X. Want, M. Kaulke, and K. Hallberg, (1999) Chap. 2.

[35] U. Schollwöck, "The density-matrix renormalization group", Reviews of modern physics **77**, 263–265 (2005).

[36] S. R. White, "Density-matrix algorithms for quantum renormalization groups", Physical Review B **48**, 10345 (1993).

[37] R. B. Lehoucq, and D. C. Sorensen, "Deflation techniques for an implicitly restarted Arnoldi iteration", SIAM Journal on Matrix Analysis and Applications **17**, 789–821 (1996).

[38] T. Nishino, "Density matrix renormalization group method for 2D classical models", Journal of the Physical Society of Japan **64**, 3598–3601 (1995).

[39] D. Tong, *Lectures on statistical physics*, (2011) `http://www.damtp.cam.ac.uk/user/tong/statphys.html` (visited on 06/07/2017).

[40] E. Ising, "Beitrag zur theorie des ferromagnetismus", Zeitschrift für Physik **31**, 253–258 (1925).

[41] S. M. Bhattacharjee, and A. Khare, "Fifty years of the exact solution of the two-dimensional ising model by onsager", Current Science **69**, 816–821 (1995).

[42] T. Nishino, and K. Okunishi, "Corner transfer matrix algorithm for classical renormalization group", Journal of the Physical Society of Japan **66**, 3040–3047 (1997).

[43] C. Huang, T. Wei, and R. Orús, "Holographic encoding of universality in corner spectra", Physical Review B **95**, 195170 (2017).

[44] R. Orús, "Exploring corner transfer matrices and corner tensors for the classical simulation of quantum lattice systems", Physical Review B **85**, 205117 (2012).

[45] I. Peschel, and V. Eisler, "Reduced density matrices and entanglement entropy in free lattice models", Journal of Physics A: Mathematical and Theoretical **42**, 504003 (2009).

[46] I. Peschel, M. Kaulke, and Ö. Legeza, "Density-matrix spectra for integrable models", Annalen der Physik **8**, 153–164 (1999).

[47] B. Davies, "Corner transfer matrices for the Ising model", Physica A: Statistical Mechanics and its Applications **154**, 1–20 (1988).

[48] K. Okunishi, Y. Hieida, and Y. Akutsu, "Universal asymptotic eigenvalue distribution of density matrices and corner transfer matrices in the thermodynamic limit", Physical Review E **59**, R6227 (1999).

[49] T. Nishino, T. Hikihara, K. Okunishi, and Y. Hieida, "Density matrix renormalization group: introduction from a variational point of view", International Journal of Modern Physics B **13**, 1–24 (1999).

[50] M. N. Barber, "Finite-size scaling", in *Phase transitions and critical phenomena*, Vol. 8, edited by C. Domb, and J. L. Lebowitz, (Academic press, 1983) Chap. 2.

[51] G. Jaeger, "The Ehrenfest classification of phase transitions: introduction and evolution", Archive for history of exact sciences **53**, 51–81 (1998).

[52] M. E. Fisher, and A. E. Ferdinand, "Interfacial, boundary, and size effects at critical points", Physical Review Letters **19**, 169 (1967).

[53] M. E. Fisher, and M. N. Barber, "Scaling theory for finite-size effects in the critical region", Physical Review Letters **28**, 1516 (1972).

[54] S. M. Bhattacharjee, and F. Seno, "A measure of data collapse for scaling", Journal of Physics A: Mathematical and General **34**, 6375 (2001).

[55] M. Andersson, M. Boman, and S. Östlund, "Density-matrix renormalization group for a gapless system of free fermions", Physical Review B **59**, 10493 (1999).

[56] M. M. Wolf, G. Ortiz, F. Verstraete, and J. I. Cirac, "Quantum phase transitions in matrix product systems", Physical Review Letters **97**, 110403 (2006).

[57] R. J. Baxter, *Exactly solved models in statistical mechanics* (Elsevier, 1982) Chap. 7.

[58] G. Vidal, J. I. Latorre, E. Rico, and A. Kitaev, "Entanglement in quantum critical phenomena", Physical Review Letters **90**, 227902 (2003).

[59] E. Ercolessi, S. Evangelisti, and F. Ravanini, "Exact entanglement entropy of the XYZ model and its sine-Gordon limit", Physics Letters A **374**, 2101–2105 (2010).

[60] I. Affleck, "Universal term in the free energy at a critical point and the conformal anomaly", Physical Review Letters **56**, 746 (1986).

[61] E. Lieb, T. Schultz, and D. Mattis, "Two soluble models of an antiferromagnetic chain", Annals of Physics **16**, 407–466 (1961).

[62] G. J. Mata, and G. B. Arnold, "Energy gap, dynamic correlations, and correlation length in two-dimensional antiferromagnets", Physical Review B **39**, 9768 (1989).

[63] P. Pfeuty, "The one-dimensional Ising model with a transverse field", Annals of Physics **57**, 79–90 (1970).

[64] P. Calabrese, and A. Lefevre, "Entanglement spectrum in one-dimensional systems", Physical Review A **78**, 032329 (2008).

[65] T. J. Osborne, and M. A. Nielsen, "Entanglement in a simple quantum phase transition", Physical Review A **66**, 032110 (2002).

[66] R. Krčmár, and L. Šamaj, "Reentrant disorder-disorder transitions in generalized multicomponent Widom-Rowlinson models", Physical Review E **92**, 052103 (2015).

[67] R. Krcmar, A. Gendiar, and T. Nishino, "Phase diagram of a truncated tetrahedral model", Physical Review E **94**, 022134 (2016).

[68] R. Krčmár, A. Gendiar, and T. Nishino, "Phase transition of the six-state clock model observed from the entanglement entropy", arXiv:1612.07611 (2016).

[69] J. M. Kosterlitz, and D. J. Thouless, "Ordering, metastability and phase transitions in two-dimensional systems", Journal of Physics C: Solid State Physics **6**, 1181 (1973).

[70] J. M. Kosterlitz, "The critical properties of the two-dimensional xy model", Journal of Physics C: Solid State Physics **7**, 1046 (1974).

[71] N. D. Mermin, and H. Wagner, "Absence of ferromagnetism or antiferromagnetism in one-or two-dimensional isotropic Heisenberg models", Physical Review Letters **17**, 1133 (1966).

[72] P. C. Hohenberg, "Existence of long-range order in one and two dimensions", Physical Review **158**, 383 (1967).

[73] J. Fröhlich, and T. Spencer, "The Kosterlitz-Thouless transition in two-dimensional abelian spin systems and the Coulomb gas", Communications in Mathematical Physics **81**, 527–602 (1981).

[74] J. Cardy, "General discrete planar models in two dimensions: duality properties and phase diagrams", Journal of Physics A: Mathematical and General **13**, 1507 (1980).

[75] J. Villain, "Theory of one-and two-dimensional magnets with an easy magnetization plane. II. the planar, classical, two-dimensional magnet", Journal de Physique **36**, 581–590 (1975).

[76] J. V. José, L. P. Kadanoff, S. Kirkpatrick, and D. R. Nelson, "Renormalization, vortices, and symmetry-breaking perturbations in the two-dimensional planar model", Physical Review B **16**, 1217 (1977).

[77] C. M. Lapilli, P. Pfeifer, and C. Wexler, "Universality away from critical points in two-dimensional phase transitions", Physical Review Letters **96**, 140603 (2006).

[78] S. Elitzur, R. B. Pearson, and J. Shigemitsu, "Phase structure of discrete abelian spin and gauge systems", Physical Review D **19**, 3698–3714 (1979).

[79] B. Nienhuis, "Critical behavior of two-dimensional spin models and charge asymmetry in the Coulomb gas", Journal of Statistical Physics **34**, 731–761 (1984).

[80] M. E. Fisher, M. N. Barber, and D. Jasnow, "Helicity modulus, superfluidity, and scaling in isotropic systems", Physical Review A **8**, 1111–1124 (1973).

[81] S. K. Baek, and P. Minnhagen, "Non-Kosterlitz-Thouless transitions for the q-state clock models", Physical Review E **82**, 031102 (2010).

[82] Y. Kumano, K. Hukushima, Y. Tomita, and M. Oshikawa, "Response to a twist in systems with Z_p symmetry: the two-dimensional p-state clock model", Physical Review B **88**, 104427 (2013).

[83] C. Chatelain, "DMRG study of the Berezinskii–Kosterlitz–Thouless transitions of the 2D five-state clock model", Journal of Statistical Mechanics: Theory and Experiment **2014**, P11022 (2014).

[84] S. K. Baek, H. Mäkelä, P. Minnhagen, and B. J. Kim, "Residual discrete symmetry of the five-state clock model", Physical Review E **88**, 012125 (2013).

[85] O. Borisenko, G. Cortese, R. Fiore, M. Gravina, and A. Papa, "Numerical study of the phase transitions in the two-dimensional $Z(5)$ vector model", Physical Review E **83**, 041120 (2011).

[86] A. F. Brito, J. A. Redinz, and J. A. Plascak, "Two-dimensional XY and clock models studied via the dynamics generated by rough surfaces", Physical Review E **81**, 031130 (2010).

[87] C.-O. Hwang, "Six-state clock model on the square lattice: Fisher zero approach with Wang-Landau sampling", Physical Review E **80**, 042103 (2009).

[88] Y. Tomita, and Y. Okabe, "Probability-changing cluster algorithm for two-dimensional XY and clock models", Physical Review B **65**, 184405 (2002).

[89] B. Bauer, P. Corboz, R. Orús, and M. Troyer, "Implementing global abelian symmetries in projected entangled-pair state algorithms", Physical Review B **83**, 125106 (2011).

[90] T. Nishino, and K. Okunishi, "A density matrix algorithm for 3D classical models", Journal of the Physical Society of Japan **67**, 3066–3072 (1998).

[91] R. Orús, and G. Vidal, "Simulation of two-dimensional quantum systems on an infinite lattice revisited: corner transfer matrix for tensor contraction", Physical Review B **80**, 094403 (2009).

[92] T. H. Hsieh, "From d-dimensional quantum to $d+1$-dimensional classical systems".

[93] M. Suzuki, "Relationship between d-dimensional quantal spin systems and $(d+1)$-dimensional Ising systems: equivalence, critical exponents and systematic approximants of the partition function and spin correlations", Progress of Theoretical Physics **56**, 1454–1469 (1976).

[94] U. Schollwöck, "The density-matrix renormalization group in the age of matrix product states", Annals of Physics **326**, January 2011 Special Issue, 96–192 (2011).

[95] R. N. C. Pfeifer, J. Haegeman, and F. Verstraete, "Faster identification of optimal contraction sequences for tensor networks", Phys. Rev. E **90**, 033315 (2014).